

# We are IntechOpen, the world's leading publisher of Open Access books Built by scientists, for scientists

6,900

Open access books available

186,000

International authors and editors

200M

Downloads

Our authors are among the

154

Countries delivered to

TOP 1%

most cited scientists

12.2%

Contributors from top 500 universities



WEB OF SCIENCE™

Selection of our books indexed in the Book Citation Index  
in Web of Science™ Core Collection (BKCI)

Interested in publishing with us?  
Contact [book.department@intechopen.com](mailto:book.department@intechopen.com)

Numbers displayed above are based on latest data collected.  
For more information visit [www.intechopen.com](http://www.intechopen.com)



## Substituents and Dopants in the Structure of Apatite

Petr Ptáček

Additional information is available at the end of the chapter

<http://dx.doi.org/10.5772/62213>

### Abstract

The structure of apatites allows large variations of composition given by the generic formula ( $M_{10}(XO_4)_6Z_2$ ) including partial or complete substitution of both the cationic as well as the anionic sites, formation of nonstoichiometric forms and solid solutions. More than half of naturally occurring elements can be accommodated by apatite structure in a significant extend. The sixth chapter of this book is divided into five sections. The first, second and the third part deals with many examples of substitution including cationic substitution of M sites, anionic substitution of X-site and anionic substitution of Z-site, respectively. The remaining two sections continue with solid solution of apatites and ends with description of trace elements and their isotopes in the structure of apatite, respectively.

**Keywords:** Apatite, Substitution, Solid solution, Trace elements, Isotopes, Complexation of Metal Cations, Diffusion

As was already said in **Chapter 1**, the generic formula of apatite ( $M_{10}(XO_4)_6Z_2$ ) enables partial or complete substitution for cationic as well as anionic sites [1],[2]:

1. Cation substitution, where  $M = Ca^{2+}, Pb^{2+}, Sr^{2+}, Mg^{2+}, Fe^{2+}, Mn^{2+}, Cd^{2+}, Ba^{2+}, Co^{2+}, Ni^{2+}, Cu^{2+}, Zn^{2+}, Sn^{2+}, Eu^{2+}, Na^+, K^+, Li^+, Rb^+, NH_4^+, La^{3+}, Ce^{3+}, Sm^{3+}, Eu^{3+}, Y^{3+}, Cr^{3+}, Th^{4+}, U^{4+}, U^{6+}$  and  $\square$ .
2. Substitution for phosphorus by one or two cations, where  $X = PO_4^{3-}, AsO_4^{3-}, SiO_4^{3-}, VO_4^{3-}, CrO_4^{3-}, CrO_4^{2-}, MnO_4^{3-}, SO_4^{2-}, SeO_4^{2-}, BeF_4^{2-}, GeO_4^{4-}, ReO_5^{3-}, SbO_3F^{4-}, SiO_3N^{5-}, BO_4^{5-}, BO_3^{3-}$  and  $CO_3^{2-}$ .
3. Z-site substitution, where  $Z = F^-, OH^-, Cl^-, O_2^-, O_3^-, NCO^-, BO_2^-, Br^-, I^-, NO_2^-, CO_3^{2-}, O_2^{2-}, O^{2-}, S^{2-}, NCN^{2-}, NO_2^{2-}$  and  $\square$ .

where  $\square$  represents the vacancy cluster [1].

Besides the monoionic substitution, the co-substitution and mutual combinations of substitutions in anionic and cationic sites (multi-ionic substitution) were also often reported [3],[4],[5],[6]. Mutual substitutions of trace elements into apatite structure brought new physicochemical, mechanical and biological properties in comparison with pure apatite or monoionic substituted apatite materials, e.g. hydroxylapatite [3].

Some substitutions can proceed only at the synthesis stage, while a limited ion exchange between solid apatite and surrounding solution can also occur. Due to their high chemical diversity and ion-exchange capabilities, apatites are considered as materials for toxic waste storage and for wastewater purification. The ion exchange in apatitic structures in human organism also presents an interest for medicine [7].

Recent studies have shown that a number of alkaline-earth-rare-earth silicates and germanates also have the apatite structure, and these have the cell sizes which span the division between the "apatites" and the "pyromorphites". Some, particularly barium and lanthanum apatites, have the lattice parameters comparable with the members of the pyromorphite group. Thus,  $\text{Ba}_2\text{La}_8(\text{SiO}_4)_6\text{O}_2$  has the cell parameters  $a = 9.76 \text{ \AA}$  and  $c = 7.30 \text{ \AA}$  and  $\text{Pb}_{10}(\text{PO}_4)_6\text{F}_2$  shows  $a = 9.76$  and  $c = 7.29 \text{ \AA}$ , while  $\text{Ba}_3\text{La}_7(\text{GeO}_4)_6\text{O}_{1.5}$  has  $a = 9.99 \text{ \AA}$  and  $c = 7.39 \text{ \AA}$  and  $\text{Pb}_{10}(\text{AsO}_4)_6\text{F}_2$  has  $a = 10.07 \text{ \AA}$  and  $c = 7.42 \text{ \AA}$ . During synthetic studies, however, it became apparent that the prediction of the composition of compounds with apatite-type structures could not be made solely on the basis of satisfying the valence considerations, since the occurrence of the apatite-type structure also appears to be determined by the ratio of the mean size of "A" ions (i.e. Ca ions in fluorapatite) to the mean size of "X" ions in  $\text{XO}_4$  [8],[9].

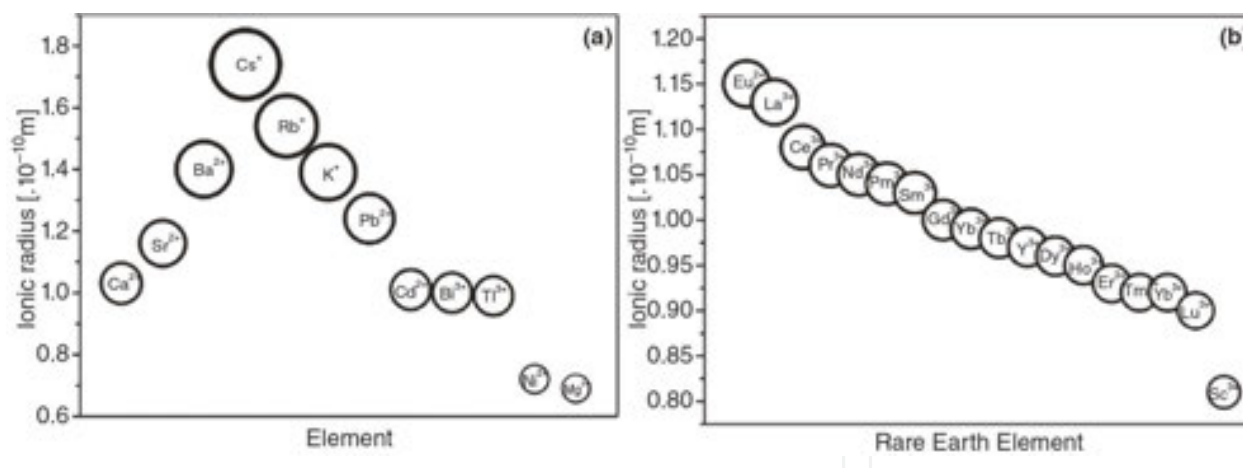


Fig. 1. The ionic radius of elements that can be accommodated instead of M in the lattice of apatite ( $\text{M}_5(\text{XO}_4)_3\text{Z}_q$ ).

The structure of hydroxyapatite allows large variations from its theoretical composition as well as the formation of nonstoichiometric forms and ionic substitutions. More than half of naturally occurring elements are known to be accommodated in the apatite lattice to significant extent.  $\text{Ca}^{2+}$  cation can be substituted by  $\text{Na}^+$ ,  $\text{K}^+$ ,  $\text{Mg}^{2+}$ ,  $\text{Sr}^{2+}$ ,  $\text{Pb}^{2+}$ ,  $\text{Mn}^{2+}$  (Fig. 1(a)) or rare-earth elements<sup>1</sup> (REE, Fig. 1(b)) and  $\text{PO}_4^{3-}$  anions by  $\text{AsO}_4^{3-}$ ,  $\text{SO}_4^{2-}$  or  $\text{CO}_3^{2-}$  without destroying the apatite structure. The changes in lattice parameters must be indicative of the type of substitution

occurring. For example,  $\text{Cl}^-$  interchange for  $\text{OH}^-$  ions causes a change to lattice parameters from  $a = 9.4214 \text{ \AA}$  and  $c = 6.8814 \text{ \AA}$  to  $6.628 \text{ \AA}$  and  $6.764 \text{ \AA}$ , respectively. Another example is the  $\text{Sr}^{2+}$  substitution for  $\text{Ca}^{2+}$ , which causes lengthening of  $a$ - and  $c$ -axes from  $9.418 \text{ \AA}$  and  $6.884 \text{ \AA}$  to  $9.76 \text{ \AA}$  and  $7.27 \text{ \AA}$ , respectively [8],[12],[13],[14],[15].

The substitutions at Z site play a very important role in the crystallography of specific species. The Z site lies in the channel formed by the X sites in fluorapatite and is of just the right size to fit between X atoms, and it lies on (001) mirror planes to yield the space group  $\text{P6}_3/\text{m}$ . When Cl substitutes for F, Cl is too large to fit on the mirror plane, so it is displaced along the  $c$ -axis and the space group becomes  $\text{P6}_3$ . The OH substitution is even more complex. OH anions are not spherically symmetric due to  $\text{H}^+$  (proton) present in the charge cloud of O atoms. H causes a displacement of O off the mirror plane, the O-H orientation tends to align in a given channel, but adjacent channels may have different displacements and orientations. The result is that well-crystallized hydroxylapatites are usually monoclinic with the space group  $\text{P2}_1/\text{m}$  or  $\text{P2}_1$  [12].

Some of the various families of substitutions that were experimentally established in apatites are summarized in **Table 1**. In general, the ions that substitute for Ca in the A position have the valences from 1 to 3 and the coordination numbers of VII at Ca(2) ( $6h$ ) site and IX at Ca(1) ( $4f$ ) site. **Table 2** introduces the cation radii of possible apatite substituents at M-site [2].

$\text{M}_{10}$	$\text{X}_6$	$\text{O}_{24}$	$\text{Z}_2$	Designation
$\text{M}(1)_4\text{M}(2)_6$		$\text{O}_{12}\text{O}_6\text{O}_6$		
$\text{Ca}_{10}$	$\text{P}_6$	$\text{O}_{24}$	$(\text{OH})_2$	HAP
$\text{C}_4\text{Ln}_6$	$\text{Si}_6$			
$\text{Sr}_{10}$	$\text{S}_3\text{Si}_3$		$\text{F}_2$	FAP
$\text{Ca}_2\text{Ln}_8$	$\text{Si}_6$		$\text{O}_2$	Oxyapatite
$\text{SrCa}_9$	$\text{P}_6$		$\square$	Z-site vacancies
$\text{Nd}_4\text{Ca}_6$	$\text{Ge}_6$		$\square_2$	
$\text{Sr}_{10}$	$\text{P}_4\text{Si}_2$		$\square_2$	
$\text{Na}_2\text{Ca}_8$	$\text{P}_6$		$\square_2$	
$\square_2\text{La}_2\text{Ca}_4\text{La}_2$			$\square_2$	M-, Z-site vacancy
$\square_2\text{La}_2\text{La}_2$	$\text{Ge}_6$		$(\text{OH})_2$	M-site vacancies (?)

**Table 1.** Structural formulas of apatites:  $\text{M}(1)_4\text{M}(2)_6(\text{XO}_4)_6\text{Z}_2$  [2].

<sup>1</sup> The minerals with essential rare-earth elements (REE or rare-earth metals, REM) or chemically related elements Y or Sc are termed as rare-earth minerals. They must be named with suffix (Levinson modifier [10],[11]), indicating the dominant rare-earth element (some examples can be found in **Chapter 1 (Table 3)**). Please see also note 2.

Substituents		Coordination number				
		Arens		Shannon and Prewitt		
		VI	VI	VII	VIII	IX
M <sup>2+</sup>	Ba	1.34	1.36	1.39	—	1.47
	Pb	1.20	1.18	—	1.29	1.33
	Eu	—	1.17	—	1.25	—
	Sn	0.93	—	—	1.22	—
	Sr	1.12	1.16	1.21	1.25	—
	Ca	0.99	1.00	1.07	1.12	1.18
	Cd	0.97	0.95	1.00	1.07	—
	Mn	—	0.83	—	0.93	—
	Zn	0.74	0.745	—	—	0.90 (E)
	Co	0.72	0.735	—	—	—
	Cu	0.72	0.73	—	—	—
	Mg	0.66	0.72	—	0.89	—
	Ni	0.69	0.69	—	—	—
M <sup>+</sup>	K	1.33	1.38	1.46 (?)	1.51 (?)	1.55 (?, E)
	Na	0.97	1.02	1.13 (?)	1.16	1.32 (?, E)

(E) and (?) denote interpolated and doubtful values, respectively.

**Table 2.** Cation radii of possible apatite substituents at M<sub>10</sub>-site of M<sub>10</sub>(XO<sub>4</sub>)<sub>6</sub>Z<sub>2</sub> unit [2].

An example of charge compensating substitution for phosphorus by two cations is the substitution during the synthesis of apatite species of the composition of Ca<sub>10</sub>(SiO<sub>4</sub>)<sub>3</sub>(SO<sub>4</sub>)<sub>3</sub>F<sub>2</sub> (CSSF, fluorellestadite [16]) [2],[17],[18]:



These synthetic phases have mineral equivalents in the minerals from the ellestadite group, which are listed in **Table 3**. Since the mineral with ideal end-member formula Ca<sub>5</sub>(SiO<sub>4</sub>)<sub>1.5</sub>(SO<sub>4</sub>)<sub>1.5</sub>Cl is assumed not to exist, the name ellestadite-(Cl) is discredited [19].

Descriptor	Brief description
<i>a</i> [Å]	Lattice constant of hexagonal unit cell
<i>b</i> [Å]	
<i>c</i> : <i>a</i>	Variable axial ratio
<i>r</i> <sub>MI</sub> [Å]	Shannon’s ionic radii of M(II)-site ion (nine-coordination)

Descriptor	Brief description
$r_X [\text{\AA}]$	Shannon's ionic radii of X-site ion
$r_{\text{MII}} [\text{\AA}]$	Shannon's ionic radii of M(II)-site ion (seven-coordination for $X = \text{F}^-$ , eight-coordination for $X = \text{Cl}^-$ and $\text{Br}^-$ )
$R_Z [\text{\AA}]$	Shannon's ionic radii of Z-site ion
$A_v \text{ CR} [\text{\AA}]$	Average crystal radius = $[(r_{\text{M(I)}}x4) + (r_{\text{M(II)}}x6) + (r_Xx6) + (r_{\text{O}}x24) + (r_Zx2)]/42$
$M_{\text{EN}} - O_{\text{EN}}$	Electronegativity difference between M and O atom
$X_{\text{EN}} - O_{\text{EN}}$	Electronegativity difference between X and O atom
$M_{\text{EN}} - Z_{\text{EN}}$	Electronegativity difference between M atom at M(II) site and Z atom
$M_{\text{EN}} - X_{\text{EN}}$	Electronegativity difference between M atom at M(I) site and X atom
$M(\text{I}) - O(1) [\text{\AA}]$	Distance between M(I) atom and O(1) atom
$M(\text{I}) - O(1)^{M(\text{I})z=0} [\text{\AA}]$	Distance between M(I) atom and O(1) atom with the constraint $z = 0$ at M(I)
$\Delta_{M(\text{I})-O} [\text{\AA}]$	Difference in the lengths $M(\text{I}) - O(1)$ and $M(\text{I}) - O(2)$ .
$\Delta_{M(\text{I})-O}^{M(\text{I})z=0}$	Difference in the lengths $M(\text{I}) - O(1)$ and $M(\text{I}) - O(2)$ with the constraint $z = 0$ at M(I)
$\Psi_{M(\text{I})-O} [^\circ]$	Angle that $M(\text{I})-O(1)$ bond makes with respect to $c$
$\Psi_{M(\text{I})-O}^{M(\text{I})z=0} [^\circ]$	Angle that $M(\text{I})-O(1)$ bond makes with respect to $c$ with the constraint $z = 0$ at M(I)
$\delta_{M(\text{I})} [^\circ]$	Counter-rotation angle of $M(\text{I})\text{O}_6$ structural unit
$\phi_{M(\text{I})} [^\circ]$	Metaprism twist angle $(\pi/3 - 2\delta_{M(\text{I})})$
$\alpha_{M(\text{I})} [^\circ]$	Orientation of $M(\text{I})_6$ unit with respect to $a$
$\langle X-O \rangle [\text{\AA}]$	Average X-O bond length
$\langle \tau_{O-X-O} \rangle [^\circ]$	Average O-X-O bond-bending angle
$\rho_{M(\text{II})} [\text{\AA}]$	M(II)-M(II) triangular side length
$M(\text{II}) - Z [\text{\AA}]$	Orientation of M(II)-M(II)-M(II) triangles with respect to $a$
$M(\text{II}) - O(3) [\text{\AA}]$	Distance between M(II) and O3 atoms
$\varphi_{O(3)-M(\text{II})-O(3)} [^\circ]$	$O(3) - M(\text{II}) - O(3)$ angle
$E_{\text{total}} [\text{eV}]$	Total energy calculated from ab initio calculations

**Table 3.** The list of 29 discrete descriptors of electronic and crystal structure parameters [23].

The fluorellestadite apatite and its solid solutions are minor components of many fluorine-mineralized clinkers. It is stable to liquidus temperature of 1240°C at which it incongruently melts to dicalcium silicate ( $2\text{CaO} \cdot \text{SiO}_2$ ) and liquid [16]. The solid-state synthesis and the luminescence properties of europium-doped fluorellestadite ( $\text{CSSF}:\text{Eu}^{2+}$ ) cyan-emitting phosphor were described by QUE et al [20]. Ellestadite apatites and their solid solutions are promising materials for the immobilization of toxic metals or hazardous fly ash [21],[22].

The general composition of silico-sulfate apatites, i.e. **ellestadites**, is  $\text{Ca}_{10}(\text{SiO}_4)_{3-x/2}(\text{PO}_4)_x(\text{SO}_4)_{3-x/2}(\text{F,Cl,OH})_2$  and their structures conform to  $\text{P6}_3/\text{M}$  hexagonal symmetry where  $\text{F}^-$  is located at the 2a (0, 0,  $\frac{1}{4}$ ) position, while  $\text{Cl}^-$  is displaced out of the 6h Ca(2) triangle plane and occupies 4e (0, 0, z) split positions with z ranging from 0.336(3) to 0.4315(3). Si/S randomly occupies the 6h tetrahedral site [19],[21].

The syntheses of Sr and Pb analogues of CSSF are also reported [18]. Strontium silico-sulfate apatite is not stable and decomposes to the mixture of strontium silicate and sulfate when heated to  $1130^\circ\text{C}$  for 30 min. Since high temperatures must be avoided, several attempts to prepare cadmium and barium silico-sulfate apatites were unsuccessful and the silicocarnotite-like phase was obtained from a mixture of the composition of  $\text{Ca}_{10}(\text{GeO}_4)_3(\text{SO}_4)_8\text{F}_2$  rather than apatite [17].

Since there is a huge potential for the substitution in apatite structure  $(\text{M}(1)_4\text{M}(2)_6(\text{XO}_4)_6\text{Z}_2)$  and for the formation of solid solution as well, the classification method enables to identify the key crystallographic parameters which can serve as strong classifiers of crystal chemistries. The structure maps for apatite compounds via data mining were reported by BALACHANDRAN and RAJAN [23]. The selection of the pair of key parameters from a large set of potential classifiers is accomplished through the linear data dimensionality reduction method. This structure can be represented as a 29-dimensional vector, where the vector components are discrete scalar descriptors (**Table 3**) of electronic and crystal structure attributes utilized for the construction of the map of apatite compounds.

Basically, the structure map approach involves the visualization of the data of known compounds with known crystal structures in a two-dimensional space using two scalar descriptors (normally heuristically chosen), which are associated with physical/chemical properties, crystal chemistry or electronic structure. The objective is to map out the relative geometric position of each structure type from which one tries to discern qualitatively if there are strong associations of certain structure types to certain bivariate combinations of parameters [23].

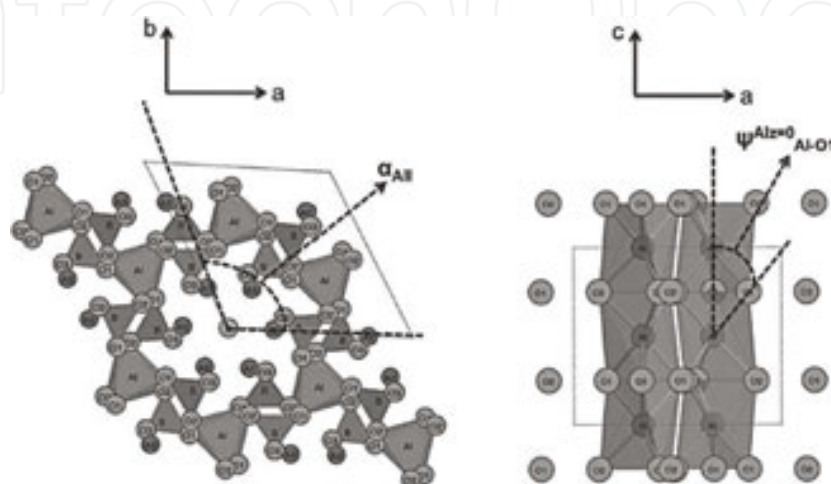




Fig. 2. Bond-distortion angle applied for the construction of structure map [23].

A new structure map, defined using the two distortion angles (Fig. 3) [23]:

1. The  $\alpha_{\text{MII}}$  (rotation angle of  $\text{M}^{\text{II}}\text{-M}^{\text{II}}\text{-M}^{\text{II}}$  triangular units);
2. The  $\psi_{\text{MI-O1}}^{\text{MIz=0}}$  (angle that  $\text{M(I)}-\text{O1}$  bond makes with the  $c$  axis when  $z = 0$  for the  $\text{M(I)}$  site).

That enables to classify the apatite crystal chemistries based on the site occupancy at M, X and Z sites and this classification is accomplished using the K-means clustering analysis (Fig. 3).

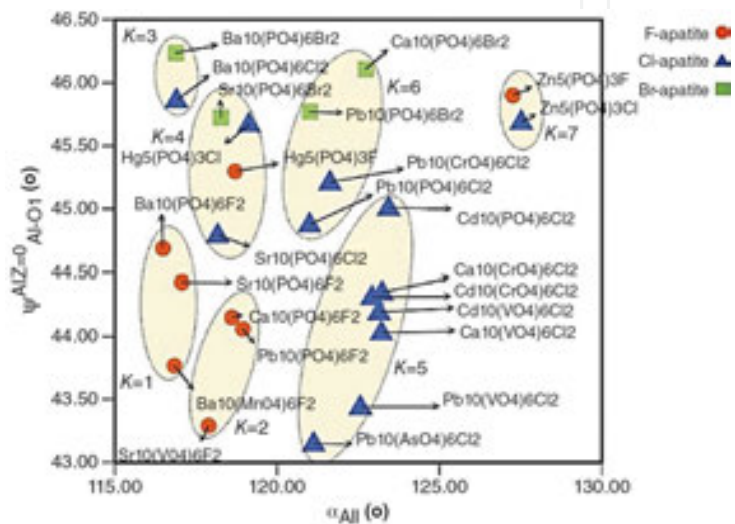


Fig. 3. Structure map for the classification of apatite chemistries based on the site occupancy (Table 4) at M, X and Z sites [23].

For example, clusters 1 and 2 ( $k = 1$  and  $k = 2$ ) correspond to F-apatites (fluorapatites). They are well localized in the structure map and are characterized by relatively low  $\alpha_{\text{MII}}$  and  $\psi_{\text{MI-O1}}^{\text{MIz=0}}$ . Two F-apatites which do not belong to the clusters  $k = 1$  and  $k = 2$  are  $\text{Hg}_5(\text{PO}_4)_3\text{F}$  (in  $k = 4$ ) and  $\text{Zn}_5(\text{PO}_4)_3\text{F}$  (in  $k = 7$ ). While the existence of fully stoichiometric  $\text{Zn}_5(\text{PO}_4)_3\text{F}$  apatite compound is uncertain due to relatively small ionic size of  $\text{Zn}^{2+}$  cations, the relative position of  $\text{Hg}_5(\text{PO}_4)_3\text{F}$  suggests some peculiar characteristics [23].

Cluster	Site occupancy		
$k = 1$ and $k = 2$	Site	M	Ba, Pb, Sr, Ca
		X	P, V, Mn
		Z	F
$k = 3$	Site	M	Ba
		X	P
		Z	Cl, Br



Cluster	Site occupancy		
$k = 4$	Site	M	Sr, Hg
		X	P
		Z	Cl, Br
$k = 5$	Site	M	Ca, Cd, Pb
		X	V, Cr, As
		Z	Cl
$k = 6$	Site	M	Ca, Pb
		X	P
		Z	Cl, Br
$k = 7$	Site	M	Zn
		X	P
Z	Z	Z	F, Cl

**Table 4.** The relationship linking various clusters shown in **Fig. 3** with the site occupancy in the apatite unit [23].

Even though  $\text{Ca}^{2+}$  and  $\text{Hg}^{2+}$  cations have roughly the same ionic size (1.18 and 1.23 Å at M(I) site), their electronegativity data indicates that Hg atoms (electronegativity value of 2 in Pauling scale) are relatively highly covalent compared to Ca atoms (electronegativity value of 1 in Pauling scale). In the structure map, this covalent character is predicted to be manifested in the bond distortion angle  $\psi_{MI-O1}^{MIz=0}$  [23].

6.1. Cationic substitution at M(1) and M(2) sites

6.1.1. Strontium-substituted apatites

$\text{Sr}^{2+}$  ion, which is larger than  $\text{Ca}^{2+}$ , is ordered almost completely into the smaller Ca(2) site in the apatite structure (**Fig. 4**). The bond valence sums of Sr ions at two sites demonstrate that Sr is severely overbonded at apatite Ca site but less at Ca(2) site. Complete ordering of Sr into Ca(2) sites has important implications for the diffusion of that element in the apatite structure. It is the subject of several recent studies. The diffusion of Sr in (001) was shown to be as rapid or even more rapid than the diffusion parallel to [001]. As there are neither sites available for Sr, which are linked in (001), nor any interstitial sites, which can contain  $\text{Sr}^{2+}$  ion, the diffusion mechanism involving the vacancies or defects or both is indicated [24].

A series of Sr-substituted hydroxyapatites,  $(\text{Sr}_x\text{Ca}_{1-x})_5(\text{PO}_4)_3\text{OH}$ , where  $x = 0.00, 0.25, 0.50, 0.75$  and 1.00, was investigated by O'DONNELL et al [25]. The lattice parameters (a and c), the unit cell volume and the density were shown to increase linearly with strontium addition and were consistent with the addition of slightly larger and heavier ion (Sr) instead of Ca. There was a slight preference for strontium to enter Ca(2) site in mixed apatites.

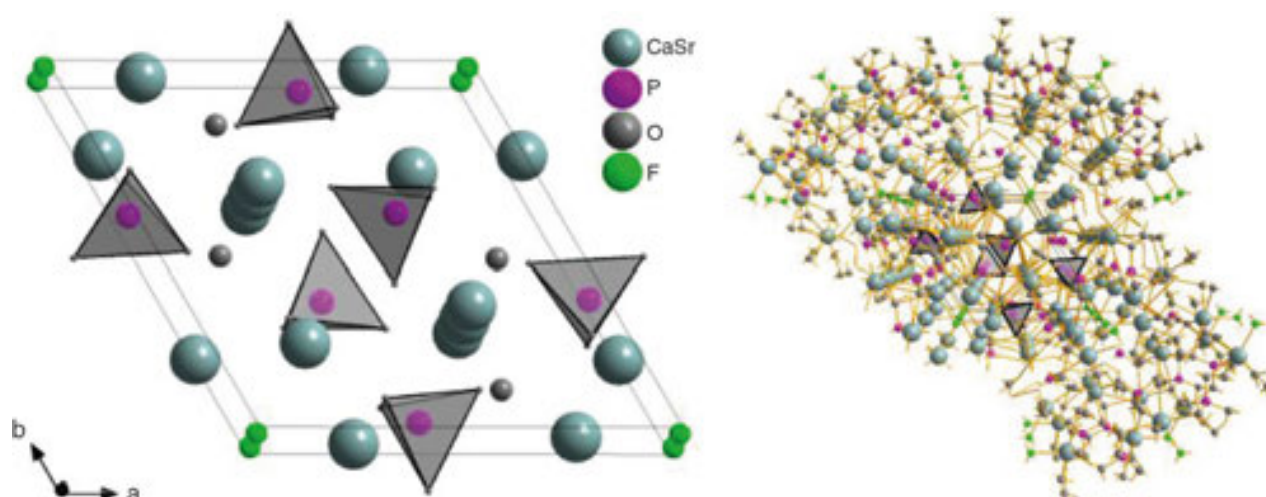


Fig. 4. The structure of natural Sr-bearing apatite refined by HUGHES et al [24] and viewed along the c-axis.

Strontium is often substituted for calcium in order to confer the radio-opacity in glasses used for dental cements, biocomposites and bioglass-ceramics. It can be concluded that strontium substitutes for calcium with little change in the glass structure as a result of their similar charge to size ratio. Glasses with low content of strontium nucleate in the bulk to form calcium apatite phase. Glasses with medium strontium content nucleate to mixed calcium-strontium apatite at the surface and glass fully substituted by strontium to strontium fluorapatite [26].

### 6.1.2. Magnesium-substituted apatite

Magnesium-substituted hydroxyapatite (MgHAP) powders with different crystallinity levels, prepared at room temperature via a heterogeneous reaction between  $\text{Mg}(\text{OH})_2/\text{Ca}(\text{OH})_2$  powders and  $(\text{NH}_4)_2\text{HPO}_4$  solution using the mechanochemical- hydrothermal route, were reported by SUCHANEK et al [27]. The as-prepared products contained unreacted  $\text{Mg}(\text{OH})_2$  and therefore had to undergo the purification in ammonium citrate aqueous solutions at room temperature. MgHAP contained 0.24 - 28.4 wt.% of Mg and the concentration of Mg was slightly lower near the surface than that in the bulk.

Two effects of different magnesium sources (magnesium nitrate and magnesium stearate) on the synthesis of Mg-substituted hydroxyapatite (Mg-n-HAP) nanoparticles by the co-precipitation method were investigated by LIJUAN et al [28]. There was no obvious difference of morphology, nanoparticle size and thermal stability between those two Mg-n-HAPs. However, Mg-n-HAP synthesized by magnesium stearate had lower crystallinity and better dispersibility, suggesting that magnesium stearate was a novel magnesium source to synthesize Mg-n-HAP, which can effectively reduce the powder crystallinity and prevent the aggregation of Mg-n-HAP nanoparticles, owing to the introduction of organic magnesium source, so as to obtain a promising candidate material to prepare Mg-n-HAP/polymer composite used in a variety of bone applications.

### 6.1.3. Copper-substituted apatites

Copper-substituted hydroxyapatite ( $\text{Ca}_{10-x}\text{Cu}_x(\text{PO}_4)_6(\text{OH})_2$  (where  $x = 0.05 - 2.0$ ) and fluorapatite  $\text{Ca}_{10-x}\text{Cu}_x(\text{PO}_4)_6\text{F}_2$  ( $x = 0.05 - 2.0$ ) were synthesized by SHANMUGAM and GOPAL [29] via the co-precipitation method and subsequent thermal treatment to  $700^\circ\text{C}$  for 30 min. Due to its antimicrobial activity, the copper-substituted fluorapatite could be applied as an antimicrobial biomaterial for various purposes like orthopedic and dental implantations.

### 6.1.4. Nickel-substituted apatites

According to MOBASHERPOU et al [30], the reaction mechanism corresponding to equimolar exchange of nickel and calcium and yielding to  $\text{Ca}_{10-x}\text{Ni}_x(\text{PO}_4)_6(\text{OH})_2$ , where  $x$  varies from 0 to 10, could be described by the following equation:



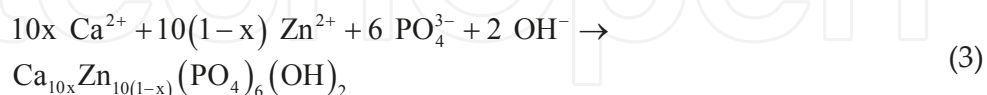
In this process,  $\text{Ni}^{2+}$  ions are first adsorbed onto the surface of hydroxyapatite (surface complexation, **Section 6.5.2**) and then the substitution of  $\text{Ca}^{2+}$  for  $\text{Ni}^{2+}$  ions takes place.

### 6.1.5. Zinc-substituted apatites

Zinc is a common bioelement. The zinc content in human bones ranges from 0.0126% to 0.0217% by weight [7]. Zinc as a cationic substituent in hydroxyapatite provides the option to counteract the effects of osteoporosis [31]. The incorporation of zinc into the HAP structure (Zn-HAP) was abundantly studied, owing to the key effect of  $\text{Zn}^{2+}$  cations in several metabolic processes that makes zinc eligible for use in many biomedical applications and to its possible antimicrobial activity [3].

The results of structure analysis indicated that Zn ions substituted partially for Ca ions in the apatite structure and the upper limit of Zn substitution for Ca in HA was about 20 mol.%. In general, the HAP lattice parameters,  $a$  and  $c$ , decreased with Zn addition [32].

Zn-substituted apatite was synthesized by the precipitation method as follows [33]:



where  $0 \leq x \leq 1$ . The pH of the solution was adjusted to 8 by aqueous solution of  $\text{NH}_3$ , and the reaction mixture was kept at  $90^\circ\text{C}$  for 5 h with stirring. The resulting suspension was then subjected to suction filtration, and the powdery product was dried at  $100^\circ\text{C}$  for 10 h. It is known that the usage of chloride or nitrate of calcium as a starting reagent may cause the incorporation of  $\text{Cl}^-$  or  $\text{NO}_3^-$  into the structure of apatite. This can be avoided by the utilization of acetate salts, because acetate ions are not incorporated into the apatite, i.e. they would not affect the apatite structure.

### 6.1.6. Iron-substituted apatites

The synthesis and the characterization of iron-substituted hydroxyapatite via a simple ion-exchange procedure were described by KRAMER et al [34]. Using a ferric chloride solution and a simple soaking procedure, FeHAP can be prepared with no apparent formation of the second phase. The substitution of  $\text{Fe}^{3+}$  into the HAP lattice results in FeHAP powders with magnetic properties. This novel simplified room temperature soaking procedure can be applied in the future to synthesize magnetic apatite-based nanoparticles for biomedical applications.

### 6.1.7. Cobalt-substituted apatites

The synthesis and the characterization of cobalt-substituted hydroxyapatite (Co-HAP) powders via the precipitation method were described by KRAMER et al [35]. Using a cobalt chloride solution and a simple soaking procedure, it is possible to prepare CoHAP with no apparent formation of second phases. Cobalt-substituted samples displayed paramagnetic properties as opposed to the diamagnetism of pure HA. The degradation studies showed that Co-HAP did not display markedly different degradation behavior from pure HAP, and the amount of cobalt released over the course of a month was extremely low, alleviating the toxicity concerns. Cobalt-substituted hydroxyapatite nanoparticles, the biomaterial with magnetic properties, could be a promising material to be used in a variety of biomedical applications, including the magnetic imaging, drug delivery or hyperthermia-based cancer treatments.

Single crystals of chlorapatite  $[\text{Ca}_5(\text{PO}_4)_3\text{Cl}]$  with the substitution of approximately 20% of  $\text{Ca}^{2+}$  by  $\text{Co}^{2+}$  (space group  $\text{P6}_3/\text{M}$ ,  $a = 9.625(3)$  and  $c = 6.747(1)$  Å,  $V = 541.3$  Å<sup>3</sup>) were prepared by ANDERSON and KOSTINER [36] via the flux techniques. Co ion is present at available six-coordinated cation site.

### 6.1.8. Manganese-substituted apatites

Naturally occurring manganese-substituted apatite is known as manganese-bearing apatite ( $\text{Mn,Ca}_5(\text{PO}_4)_3\text{F}$ , **Section 1.1**). According to the findings of HUGHES et al [24], the symmetry of Mn-bearing apatite does not degenerate from  $\text{P6}_3/\text{M}$  to  $\text{P6}$  or  $\text{P3}$  with Mn substitution, nor degenerates the symmetry limit of Mn substitution to one atom/unit cell.  $\text{Mn}^{2+}$  substituent, which is smaller than  $\text{Ca}^{2+}$ , preferentially occupies larger apatite Ca(1) site although not completely. Mn atom is underbonded at Ca site, less so at larger Ca(1) site; nine O atoms coordinating that site satisfy more effectively the Mn bond valence than seven ligands coordinating Ca(2) site. The M-O bond lengths of Mn-substituted sites reflect the substitution of the smaller Mn ion.

It is interesting to note that apatite acts effectively as a geochemical sieve that traps  $\text{Mn}^{2+}$  and excludes  $\text{Fe}^{2+}$  elements, which are virtually inseparable in most geochemical systems. The bond valence sums for  $\text{Fe}^{2+}$  at apatite Ca sites yield 1.26 and 1.19 valence units for Ca(1) and Ca(2) sites, respectively; large discrepancy from the formal valence prohibits extensive substitution of  $\text{Fe}^{2+}$  in the apatite structure (**Fig. 5**) [24].

The crystal structure of pale blue transparent Mn-rich fluorapatite (9.79 wt.% of MnO) with optimized formula  $(\text{Ca}_{8.56}\text{M}^{2+}_{1.41}\text{Fe}^{2+}_{0.01})\text{P}_6\text{O}_{24}\text{F}_2$  was resolved by HUGHES et al [24] to be of the

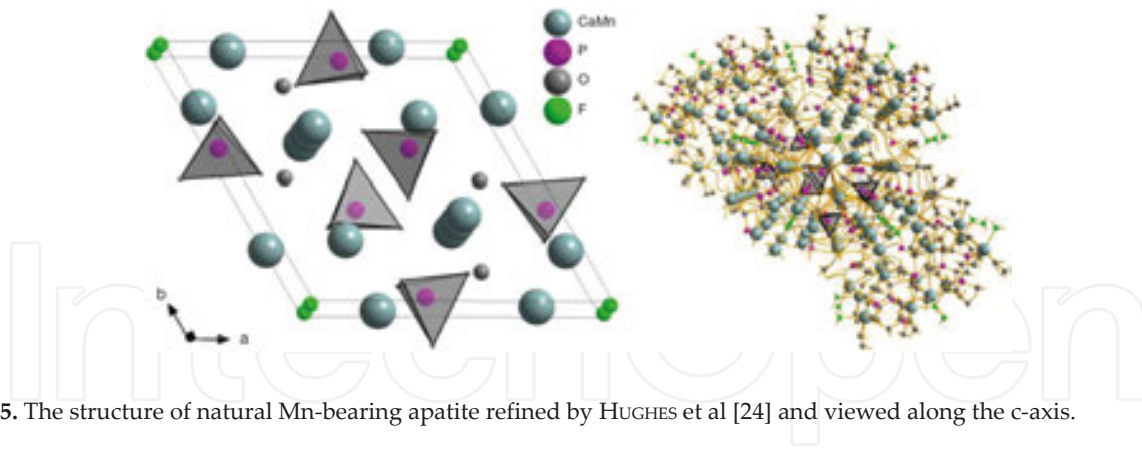


Fig. 5. The structure of natural Mn-bearing apatite refined by HUGHES et al [24] and viewed along the c-axis.

space group of  $P6_3/M$  with the cell parameters  $a = 9.3429 \text{ \AA}$ ,  $c = 6.8110 \text{ \AA}$  and  $Z = 2$ . Mn is strongly ordered at Ca(1) site ( $\text{Ca}(1)_{0.72}\text{Mn}_{0.28}$ ,  $\text{Ca}(2)_{0.96}\text{Mn}_{0.04}$ ). The apatite structure also contains  $\text{Mn}^{5+}$  at X-site ( $\text{P}_{5.96}\text{Mn}^{5+}_{0.04}$ ).

### 6.1.9. Substitution of REEs in apatite

Crystals of La-, Gd- and Dy-bearing fluorapatite [La-FAP, Gd-FAP, Dy-FAP,  $\text{Ca}_{10-x-2y}\text{Na}_y\text{REE}_x(\text{P}_{1-y}\text{Si}_x\text{O}_4)_2\text{Z}_2$ , where  $x = 0.24 - 0.29$  and  $y = 0.32 - 0.36$ ] were synthesized by hydrothermal route by FLEET and PAN [37]. The substitution of trivalent REE in apatite is principally compensated as follows:



The structure of some REE-bearing apatites [37],[38] is shown in Fig. 6.

The partitioning of REE between two Ca positions in apatite contradicts usual first-order dependence on spatial accommodation, with LREE<sup>3</sup> [39],[40],[41],[42],[43], in particular, favoring the smaller Ca(2) position. This behavior was variously ascribed to the control via [37]:

<sup>2</sup> Rare-earth elements or metals (REE or REM) are Sc, Y and lanthanoids [40]. Light rare-earth elements (LREE) are Sc, La, Ce, Pr, Nd, Pm, Sm, Eu and Gd (7 elements from La to Eu are known as the cerium group or cerium-group lanthanides). Heavy rare-earth elements (HREE) are Y, Tb, Dy, Ho, Er, Tm, Yb and Lu. The definition of LREE and HREE is based on the electron configuration. LREEs possess unpaired 4f electron from 0 to 7 (half-filled 4f electron shell). HREEs have paired electron (the clockwise and counterclockwise spinning electron) [39],[41]. The element with half-filled f-electron shell (Eu) shows enhanced stability of its particular electron configuration [43]. In some cases, REEs are divided into three groups including (1) LREE (La – Pm), (2) MREE (middle rare-earth element, Sm – Dy) and (3) HREE (Ho – Lu) [42].



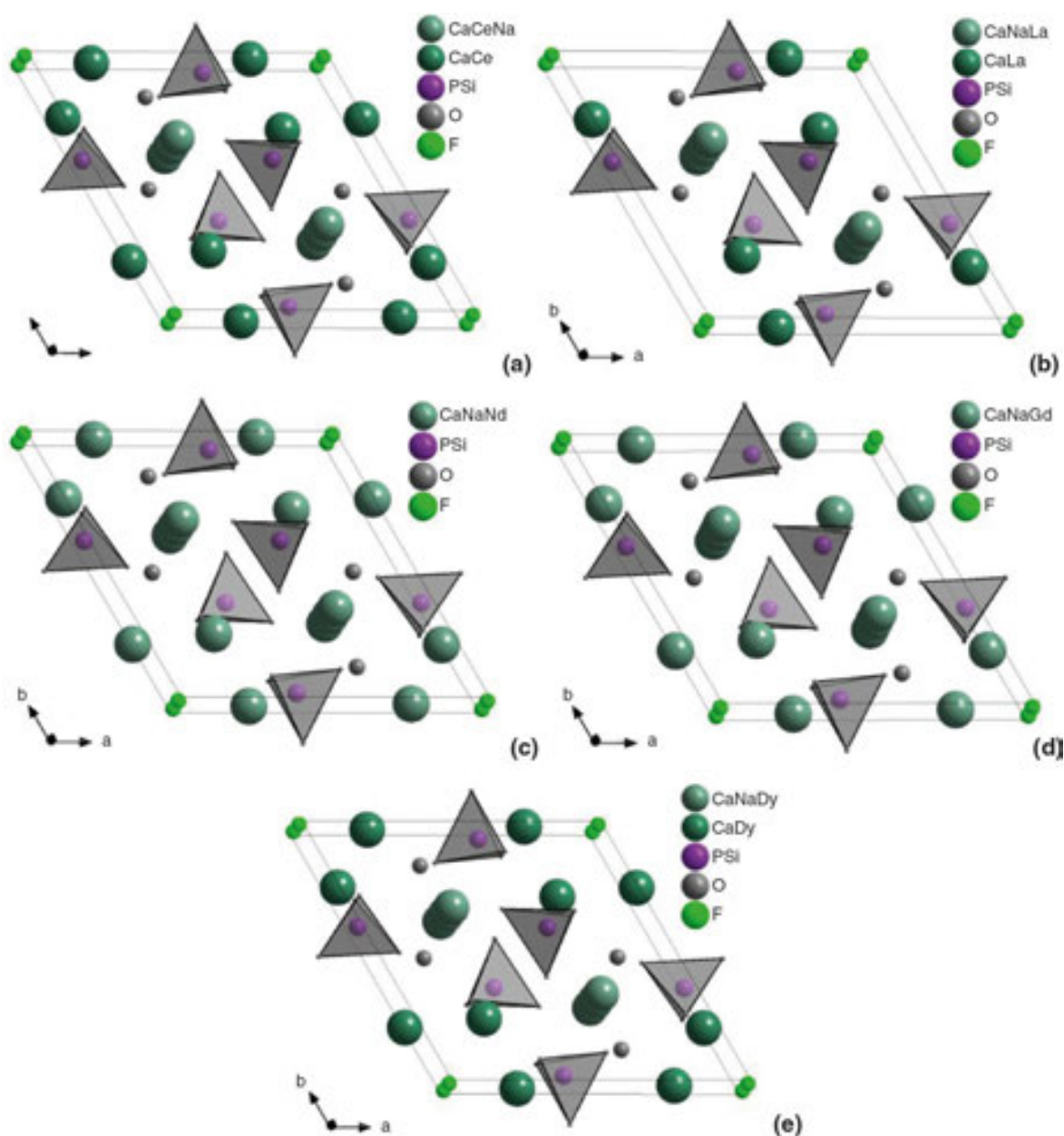


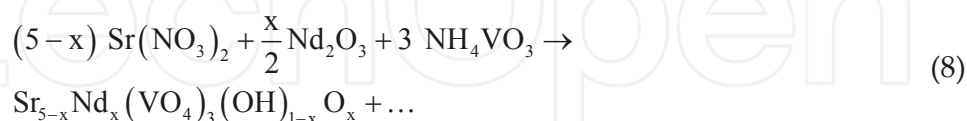
**Fig. 6.** Rare-earth-element ordering and structural variations in natural rare-earth-bearing fluorapatites (a), LaFAP (b), NdFAP (c), GdFAP (d) and DyFAP (e) [37],[38].

- i. Substitution mechanism;
- ii. Electronegativity difference;
- iii. Bond valence.

The preference of individual REE among multiple Ca positions in minerals (the site occupancy of individual REE) was not extensively studied because of the inability of conventional diffraction methods to distinguish among individual elements at multiply-occupied sites. The site preference for individual LREE from theoretical bond-valence sums was estimated by

HUGHES et al [38], reasoning that  $\text{La} \rightarrow \text{Pr}$  should preferentially substitute into  $\text{Ca}(2)$ , whereas  $\text{Pm} \rightarrow \text{Sm}$  should selectively substitute into  $\text{Ca}(1)$ .

The isomorphic substitutions of neodymium for strontium in the structure of synthetic  $\text{Sr}_5(\text{VO}_4)_3\text{OH}$  apatite structure type ( $\text{P6}_3/\text{M}$ ) were reported by GET'MAN et al [44]. The synthesis of apatite specimen was performed via the solution thermolysis on the assumption of the following reaction:



where  $x = 0, 0.02, 0.08, 0.10, 0.12, 0.14, 0.16, 0.18$  and  $0.20$ . The substitution scheme can be expressed as:



The procedure includes three stages:

- a. Preparation of solution;
- b. Thermolysis;
- c. Treatment of the dry residue.

The solutions for the thermolysis were prepared by dissolving  $\text{Sr}(\text{NO}_3)_2$  in water;  $\text{Nd}_2\text{O}_3$  was dissolved in water with nitric acid added;  $\text{NH}_4\text{VO}_3$  was dissolved in water with hydrogen peroxide added. Dry residues after concentrating the solutions were pestled in an agate mortar and calcined with the temperature steadily raised from  $600$  to  $800^\circ\text{C}$  and intermittent grindings [44].

#### 6.1.10. Actinides-bearing apatites

Thorium and uranium (actinides [45],[46]<sup>3</sup>)-bearing apatites were synthesized by LUO et al [47] from doped phosphate-halide-rich melts. The structure refinements (**Fig. 7**) of U-doped fluorapatites indicate that U substitutes almost exclusively into  $\text{Ca}(2)$  site with the site occupancy ratios  $\text{UCa}(2)/\text{UCa}(1)$ , which range from  $5.00$  to  $9.33$ . Similarly, the structure refinements of Th-doped fluorapatites indicate that Th substitutes dominantly into  $\text{Ca}(2)$  site with  $\text{ThCa}(2)/\text{ThCa}(1)$  values, which range from  $4.33$  to  $8.67$ .

<sup>3</sup> The actinides occupy the second row of the f-block in the periodic table. The actinide group or actinoids (An) include 14 elements with atomic numbers from  $90$  (Th) to  $103$  (Lr) [43]. The elements with atomic numbers greater than  $92$  (U) are termed as transuranics. The elements with atomic numbers greater than  $100$  are named as the super-heavy elements (SHE). There is also the concept of the periodic table developed by G.T. SEABORG predicting a new inner transition series of 32 elements (from  $122$  to  $153$  element), called the superactinide series [45],[46]. Only actinium, thorium, uranium and (in trace quantities) protactinium and plutonium are primordial, while the elements from neptunium onwards are present on Earth solely through artificial generation [46].



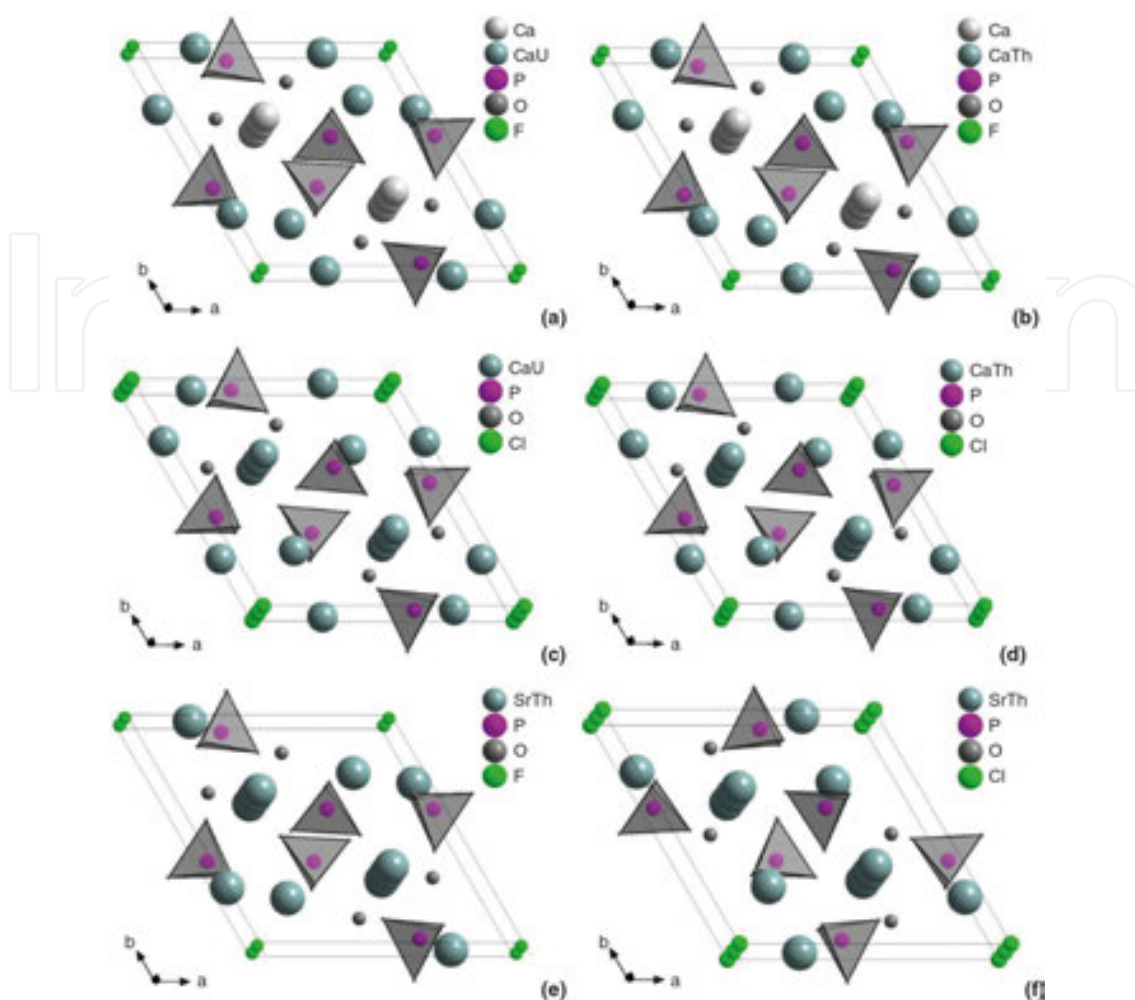
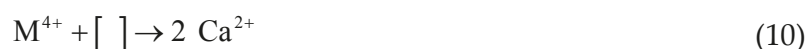


**Fig. 7.** The structure of UFAP (a), ThFAP (b), UClAP (c), ThClAP (d), ThSrFAP (e) and ThSrClAP (f) [47] viewed along the *c*-axis.

The structure refinements of U-doped chlorapatites show that U is essentially distributed equally between the two Ca sites with  $UCa(2)/UCa(1)$  values, which range from 0.89 to 1.17. The results of Th-doped chlorapatites show that Th substitutes into both Ca(1) and Ca(2) sites with  $ThCa(2)/ThCa(1)$  values, which range from 0.61 to 0.67. In Th-doped strontium apatites with F and Cl end-members, Th is incorporated into both Ca(1) and Ca(2) sites. The range of  $ThCa(2)/ThCa(1)$  values is 0.56 to 1.00 for the F end-member and 0.39 to 0.94 for the Cl end-member. U-doped samples indicate that U in fluorapatite is tetravalent, whereas, in chlorapatite, it is heterovalent but dominantly hexavalent [47].

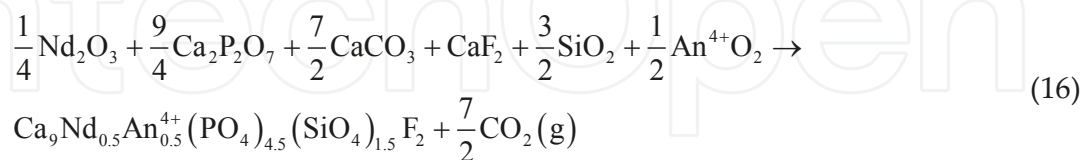
Based on the chemical analyses of U-, Th-doped fluor-, chlor- and strontiumapatite specimens in this study, local charge compensation may be maintained by the following coupled substitutions (M represents U or Th and [ ] represents the vacancy) [47]:



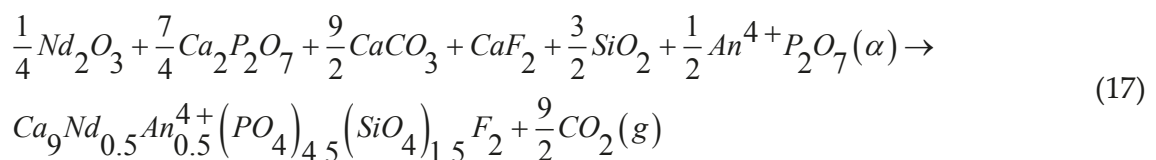


The incorporation of U and Th into fluorapatite results in a decrease of the size of both Ca polyhedra, but the incorporation of U and Th into chlorapatite gives rise to an increase in the volume of both Ca polyhedra. The decrease of both Ca polyhedral volumes in fluorapatite caused by the substitution of U and Th can be explained by the decrease of ionic radius from Ca to U and Th. However, the increase in the volume of both Ca polyhedra in chlorapatite is hard to understand. Because of the effect on Ca(2) polyhedron caused by the replacement of F<sup>-</sup> by Cl<sup>-</sup>, it can be explained by the structural distortion of Ca(2) polyhedron [47].

Uranium-doped oxy-silicophosphates (britholites) of the composition of  $Ca_xLa_y(SiO_4)_{6-u}(PO_4)_uO_t:U^{4+}$  were synthesized by RIADH et al [48] via the high-temperature solid-state reaction. The uranium solubility limit was found to be comprised between 4.6 and 4.8 mol.%. The investigation of uranium heated to 1200°C led to the uranium diffusion coefficient of  $2.14 \cdot 10^{-14} m^2 \cdot s^{-1}$ . The synthesis and the characterization of uranium- ( $Ca_9Nd_{1-x}U_x(PO_4)_{5-x}(SiO_4)_{1+x}F_2$ ) and thorium-bearing britholites ( $Ca_9Nd_{1-x}Th_x(PO_4)_{5-x}(SiO_4)_{1+x}F_2$ ) were also reported by TERRA et al [49],[50]:



or



where  $An^{4+}$  substitutes for tetravalent  $U^{4+}$  and  $Th^{4+}$ .

The incorporation of thorium in the structure is probably possible due to small differences of ionic radius between calcium (1.06 Å), neodymium (1.05 Å) and thorium (1.00 Å). In order to ensure the quantitative incorporation of thorium, it appeared necessary to consider the coupled substitution [50].



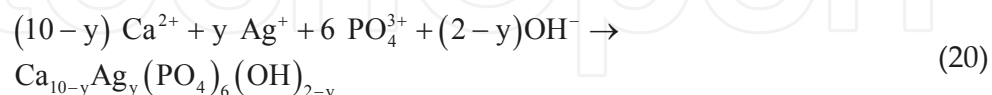
instead of the substitution scheme:



Indeed, in the first way, homogeneous and single-phase solid solutions were prepared from  $Ca_9Nd(PO_4)_5(SiO_4)F_2$  to  $Ca_9Th(PO_4)_4(SiO_4)_2F_2$  leading to full neodymium substitution. Associated small increase of the unit cell parameters results from the simultaneous replacement of phosphate groups by bigger silicate. It was accompanied by a significant change in the grain morphology. These results contrast with those obtained when the coupled substitution according to Eq. 19 was performed, which confirmed the limitation of about 10 wt.% in the Th substitution [50]. Good resistance of the materials to influence of aqueous solutions enables their utilization for the immobilization of tetravalent actinides in phosphate ceramics [49].

#### 6.1.11. Silver-substituted apatite

The favorable biocompatibility of hydroxyapatite (HA) makes it a popular bone graft material as well as a coating layer on metallic implant. One common and accepted strategy to prevent the implant-related infections is to create antibacterial properties for the implant. Silver ions can be either incorporated into the apatite during the co-precipitation process (AgHAP-CP) or subjected to the ion exchange with calcium ions in apatite (AgHAP-IE). The incorporation of silver ions into apatite is based on the equation [51]:



where  $y$  is the molar amount of silver to be incorporated. However, the distribution of silver ions in AgHAP-CP and AgHAP-IE was different, thus affecting the antibacterial action.

#### 6.1.12. Cadmium-substituted apatites

The absorption of cadmium cations in apatites is relevant both from the medical standpoint of cadmium uptake by human bones, as well as since cadmium migration in nature involves

the absorption and desorption equilibria with natural minerals, including apatites. Cadmium has a slight preference for Ca(I) site in fluorapatite and for Ca(II) site in hydroxyapatite [7], [52]. The interactions between these two ions (Cd and Ca) during absorption and ionic change processes in apatites present therefore considerable practical and theoretical interest. Cadmium is also a frequent heavy toxic pollutant element in water [7].

Calculated energy differences ( $E$ ) between these sites are of 12 and 8 kJ·mol<sup>-1</sup> for fluorapatite and hydroxylapatite, respectively. The preference is not strong, and however, a part of the sites of the other type is also occupied by cadmium ions. The relative site occupation can be expressed by the equation [7]:

$$P = \frac{\text{probability of substitution at Ca(1) site}}{\text{probability of substitution at Ca(2) site}} = \frac{4}{6} \exp\left(-\frac{E}{kT}\right) \quad (21)$$

where  $E = E(\text{Cd}^{2+} \text{ or } \text{Zn}^{2+} \text{ on Ca(1)}) - E(\text{Cd}^{2+} \text{ or } \text{Zn}^{2+} \text{ on Ca(2)})$ . At  $T = 298 \text{ K}$ ,  $P = 85$  and  $17$   $\text{Cd}^{2+}$  in fluorapatite and hydroxylapatite, respectively. From the value of  $P$  and from the fact that the sum of the two probabilities is 1, one can calculate that the probability of the lower-energy site occupancy is of 99% and 94%, respectively.

BADRAOUI et al [53] reported that the maximum amount of cadmium substitution for strontium in the system  $\text{Sr}_{10-x}\text{Cd}_x(\text{PO}_4)_6\text{Z}_2$  ( $\text{Z} = \text{OH}$  and  $\text{F}$ ) accounts for about 40 at% in HAP and for 60 at% in FAP. The increase of cadmium content induces stronger decrease of the c-axis with respect to the a-axis. The structure refinements evidence found a statistical distribution of Cd atoms in  $\text{Sr}_{10-x}\text{Cd}_x(\text{PO}_4)_6(\text{OH})_2$  and a light preference for M(1) site in  $\text{Sr}_{10-x}\text{Cd}_x(\text{PO}_4)_6(\text{F})_2$ . The stability of the system  $\text{M}_{10-x}\text{M}'_x(\text{PO}_4)_6\text{Z}_2$  ( $\text{M}$  and  $\text{M}' = \text{Ca}, \text{Pb}, \text{Cd}, \text{Sr}$  and  $\text{Z} = \text{OH}$  and  $\text{F}$ ) is strongly affected by the polarizability. As a matter of fact, complete miscibility is possible even when the cations exhibit great size differences, provided they are not both soft acids. Otherwise, the presence of two cations with quite different radii and relevant polarizabilities induces important distortions of the apatite unit cell and  $\text{PO}_4$  tetrahedra and consequently limits the possibility of mutual substitution.

## 6.2. Anionic substitution at X-site

Pentavalent arsenic, vanadium and chromium substitution can completely replace phosphorus in calcium, strontium and barium fluor- and chlorapatites. Calcium fluor-vanadate, -arsenate and -chromate structures were distorted compared to normal hexagonal apatite. Manganese completely replaced phosphorus only in barium apatites, while chromium and manganese could not be incorporated into lead apatites. Excluding these exceptions, continuous solid solutions were formed between the phosphate and/or vanadate and the chromate or manganese analogues for given divalent and halide ions [54]. The substitution of  $\text{CO}_3^{2-}$  ions at X- (carbonate-apatite of A-type) and Z-site (carbonate-apatite of B-type) was already described in Section 4.6.

### 6.2.1. Arsenate substitution in hydroxylapatite

The arsenate ( $\text{As}^{5+}$ ) substitution in the hydroxylapatite structure was examined by LEE et al [55]. The investigation with samples of hydroxylapatite, the  $\text{As}^{5+}$ -substituted analogue (synthetic analogue of mineral johnbaumite, **Section 1.6.3**) and of intermediate compositions does not provide any evidence of lowering the symmetry below  $\text{P6}_3/\text{M}$ . A series of arsenate-substituted hydroxyapatite was also prepared through aqueous precipitation method by ZHU et al [56]. Prepared solid solutions ( $\text{Ca}_5(\text{P}_x\text{As}_{1-x}\text{O}_4)_3(\text{OH})$ ) showed apatite structure for the whole arsenate/phosphate series. With decreasing arsenate content, the particles changed from smaller needle-like to large tabular crystals and the unit cell dimensions  $a$  and  $c$  increased but not in fair agreement with Vegard's law<sup>4</sup> [57]. In FT-IR spectra, the area of phosphate peak was gradually suppressed and the area of arsenate peak increased as the proportion of arsenate increased.

Complete  $\text{PO}_4^{3-} \leftrightarrow \text{AsO}_4^{3-}$  substitution was also recognized in experimental studies of apatite analogues, such as in the system  $\text{Sr}_5(\text{PO}_4)_3\text{OH}$ - $\text{Sr}_5(\text{AsO}_4)_3\text{OH}$  [58]. The Rietveld refinement of  $\text{Sr}_5(\text{AsO}_4)_3\text{Cl}$  (pentastrontium tris[arsenate(V)] chloride,  $890.31 \text{ g}\cdot\text{mol}^{-1}$ ) from high-resolution synchrotron data was performed by BELL et al [59]. The hexagonal compound crystallizes in the same structure (**Fig. 8**) as other halogenoapatites in the space group  $\text{P6}_3/\text{M}$  with the cell parameters:  $a = 10.1969 \text{ \AA}$ ,  $c = 7.28108 \text{ \AA}$ ,  $V = 655.63 \text{ \AA}^3$ ,  $c:a = 0.7140$  and  $Z = 2$ . The structure consists of isolated tetrahedral  $\text{AsO}_4^{3-}$  anions (As atom and two O atoms have m-symmetry), separated by two crystallographically independent  $\text{Sr}^{2+}$  cations, which are located on mirror planes and threefold rotation axes, respectively. One Sr atom is coordinated by nine O atoms and the other one by six. Chloride anions (site symmetry  $\bar{3}$ ) are at  $2a$  sites and are located in the channels of the structure.

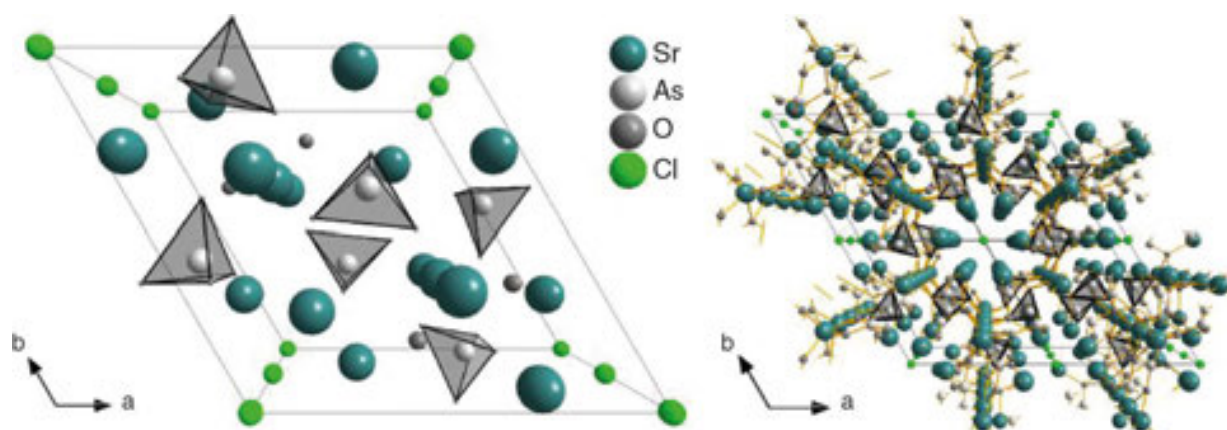


**Fig. 8.** The structure of  $\text{Sr}_5(\text{AsO}_4)_3\text{Cl}$  apatite (perspective view along the  $c$ -axis).

<sup>4</sup> Vegard's law, first pronounced in 1921, states that the lattice parameter of a solid solution of two phases with similar structures is a linear function of lattice parameters of the two end-members [57].



### 6.2.2. Vanadate substitution in hydroxylapatite

The synthesis of synthetic alkaline-earth vanadate hydroxylapatites from hydroxide fluxes was performed by MUGAVERO et al [60]. The hexagonal  $\text{Sr}_5(\text{VO}_4)_3\text{OH}$  apatite (pentastrontium tris[vanadate(V)] hydroxide, **Fig. 9(a)**) possesses the  $\text{P6}_3/\text{M}$  space group with the cell parameters:  $a = 10.0570 \text{ \AA}$ ,  $c = 7.4349 \text{ \AA}$ ,  $c:a = 0.7393$  and  $V = 651.24 \text{ \AA}^3$ . The structure of  $\text{Ba}_5(\text{VO}_4)_3\text{OH}$  (pentabarium tris[vanadate(V)] hydroxide) apatite is shown in **Fig. 9(b)**. It crystallizes in hexagonal system with the space group  $\text{P6}_3/\text{M}$  and the cell parameters:  $a = 10.4589 \text{ \AA}$ ,  $c = 7.8476 \text{ \AA}$ ,  $c:a = 0.7503$  and  $V = 743.43 \text{ \AA}^3$ .

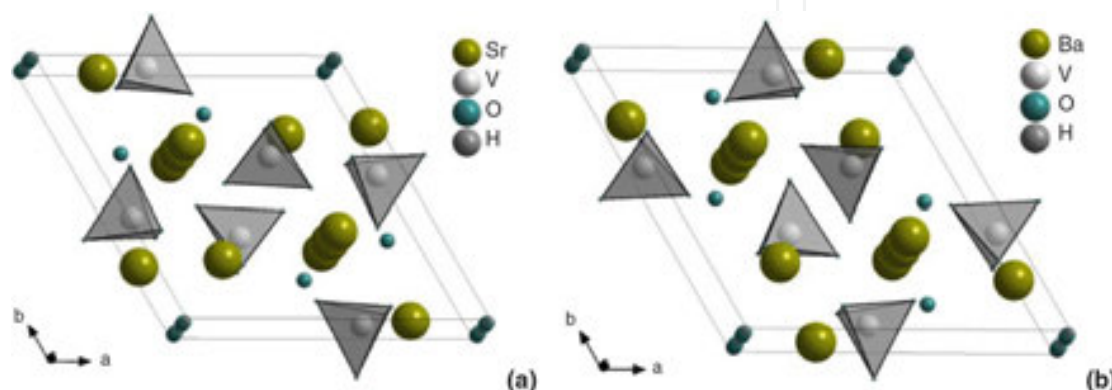


**Fig. 9.** The structure of  $\text{Sr}_5(\text{VO}_4)_3\text{OH}$  (a) and  $\text{Ba}_5(\text{VO}_4)_3\text{OH}$  (b) apatite viewed along the  $c$ -axis.

The compounds (solid solution) of the composition of  $\text{Pb}_5(\text{P}_x\text{V}_{1-x}\text{O}_4)_3\text{Cl}$  ( $0 \leq x \leq 1$ ), which are synthetic analogues of minerals pyromorphite, vanadinite and endlichite, were synthesized for the first time by CHERNORUKOV et al [61] via high-temperature solid-phase reactions:

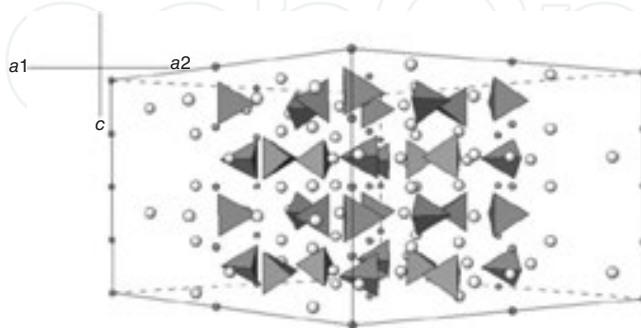
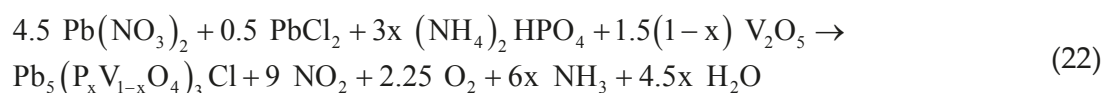


**Fig. 10.** Fragment of  $\text{Pb}_5(\text{VO}_4)_3\text{Cl}$  crystal structure [61].

The variations of unit cell parameters as a function of composition respect Vegard's law. These compounds are structurally built of discrete phosphate or vanadate tetrahedra linked to one

another by lead polyhedra, which form joint layers (**Fig. 10**). Apatite-type structures offer typically two crystallographic positions for cations differing in the coordination number and local symmetry. Lead atoms occupying the first positions form polyhedra shaped as three-capped trigonal prisms of  $\text{PbO}_6$  having the symmetry  $C_3$ , the columns of which run along the threefold axis. Distorted two-capped trigonal prisms of  $\text{PbO}_6\text{Cl}_2$  residing in the second positions have local symmetry  $C_1$ .

### 6.2.3. Chromium analogues of apatite

The syntheses of chromium (Cr(V) [62]) analogues of apatite were described in literature including the following compounds [63],[64],[65],[66],[67],[67],[69],[70],[71],[72]:

- $\text{Ca}_5(\text{CrO}_4)_3\text{OH}$ , which is isomorphous to hydroxyapatite (**Section 1.5.2**): space group  $\text{P6}_3/\text{M}$ ,  $a = 9.683 \text{ \AA}$  and  $c = 7.010 \text{ \AA}$ ,  $a:c = 1:0.7239$ ,  $V = 569.20 \text{ \AA}^3$ ,  $Z = 2$ .
- $\text{Sr}_5(\text{CrO}_4)_3\text{OH}$  with predicted lattice constants  $a = 9.9561 \text{ \AA}$  and  $c = 7.488 \text{ \AA}$ .
- $\text{Ba}_5(\text{CrO}_4)_3\text{OH}$ .
- $\text{Ca}_5(\text{CrO}_4)_3\text{F}$  with predicted lattice constants  $a = 9.733 \text{ \AA}$  and  $c = 7.0065 \text{ \AA}$
- $\text{Ca}_5(\text{CrO}_4)_3\text{Cl}$  with predicted lattice constants  $a = 10.1288 \text{ \AA}$  and  $c = 6.7797 \text{ \AA}$ .
- $\text{Sr}_5(\text{CrO}_4)_3\text{F}$  with predicted lattice constants  $a = 9.9349 \text{ \AA}$  and  $c = 7.5037 \text{ \AA}$ .
- $\text{Sr}_5(\text{CrO}_4)_3\text{Cl}$  with lattice constant  $a = 10.125 \text{ \AA}$  and  $c = 7.328 \text{ \AA}$ .
- $\text{Sr}_5(\text{CrO}_4)_3\text{Br}$  with predicted lattice constants  $a = 10.2895 \text{ \AA}$  and  $c = 7.2712 \text{ \AA}$ .

These compounds are in general prepared by the ignition of mixture of alkaline-earth carbonates, hydroxides or oxides with  $\text{Cr}_2\text{O}_3$  in the presence of water vapor.  $\text{Ca}_3(\text{CrO}_4)_2$  compound (orthochromate), which is isomorphous with  $\text{Ca}_3(\text{PO}_4)_2$ , is formed as an intermediate by carrying out the synthesis in dry atmosphere; this compound is often identified as  $9\text{CaO} \cdot 4\text{CrO}_3 \cdot \text{Cr}_2\text{O}_3$  [63],[73],[74],[75].

Theoretical compositions and formula weights of chromium apatite analogues are given in **Table 5**.

Compound	Composition [wt.%]					M [g.mol <sup>-1</sup> ]
	M	Cr	O	Z	H	
$\text{Ca}_5(\text{CrO}_4)_3\text{OH}$	35.44	27.59	36.79	—	0.18	565.39
$\text{Sr}_5(\text{CrO}_4)_3\text{OH}$	54.55	19.42	25.90	—	0.13	803.09
$\text{Ba}_5(\text{CrO}_4)_3\text{OH}$	65.29	14.83	19.78	—	0.10	1051.64
$\text{Ca}_5(\text{CrO}_4)_3\text{F}$	35.32	27.49	33.84	3.35	—	567.38
$\text{Ca}_5(\text{CrO}_4)_3\text{Cl}$	34.33	26.72	32.88	6.07	—	583.33
$\text{Sr}_5(\text{CrO}_4)_3\text{F}$	54.42	19.37	23.85	2.36	—	805.08



Compound	Composition [wt.%]					M
	M	Cr	O	Z	H	[g.mol <sup>-1</sup> ]
Sr <sub>5</sub> (CrO <sub>4</sub> ) <sub>3</sub> Cl	53.33	18.99	23.37	4.31	—	821.53
Sr <sub>5</sub> (CrO <sub>4</sub> ) <sub>3</sub> Br	50.59	18.01	22.17	9.23	—	865.98

**Table 5.** Theoretical compositions of chromium apatite analogues (M(CrO<sub>3</sub>)<sub>4</sub>Z).

Sr<sub>10</sub>(CrO<sub>4</sub>)<sub>6</sub>F<sub>2</sub> possesses typical hexagonal structure of apatite with the space group P6<sub>3</sub>/M, which was refined using the powder neutron diffraction (**Fig. 11**) for the first time by BAIKIE et al [71]. As other chromium analogues of apatite, the material contains chromium in +5 (pentavalent) oxidation state. The material shows the paramagnetic behavior.

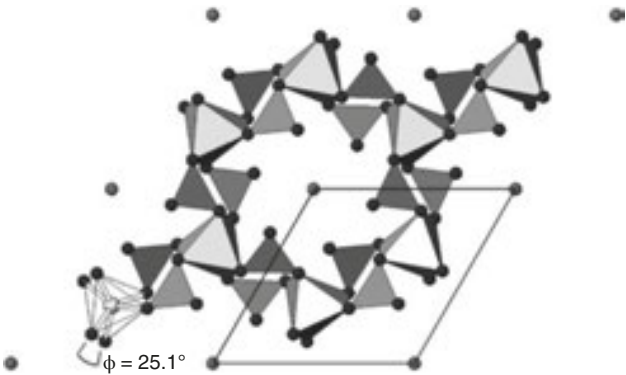


**Fig. 11.** Structural representation of Sr<sub>10</sub>(CrO<sub>4</sub>)<sub>6</sub>F<sub>2</sub> apatite with SrO<sub>6</sub> octahedra and CrO<sub>4</sub> tetrahedra: larger and smaller spheres mark F and O atoms, respectively. The unit cell is indicated by black lines [71].

The crystal structure (**Fig. 12**) and the magnetic properties of strontium chromate phase (Sr<sub>5</sub>(CrO<sub>4</sub>)<sub>3</sub>(Cu<sub>0.586</sub>O)) with apatite-like structure were determined by TYUTYUNNIK and BAZUEV [76]. The sample was prepared by solid-state synthesis via the thermal treatment of the mixture of stoichiometric amount of SrCO<sub>3</sub>, Cr<sub>2</sub>O<sub>3</sub> and CuO at the temperature of 1200°C in air for 36 h.

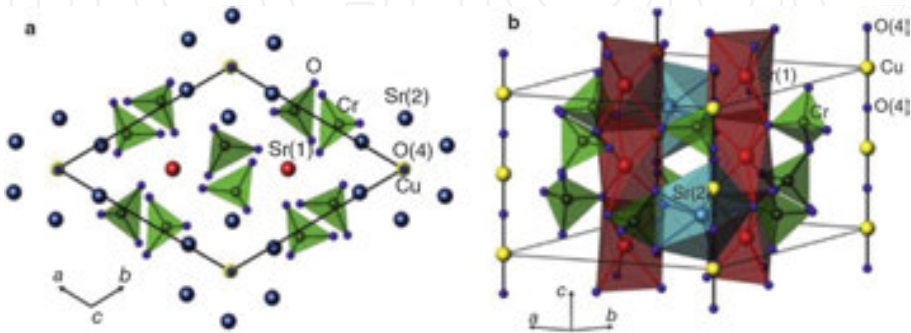


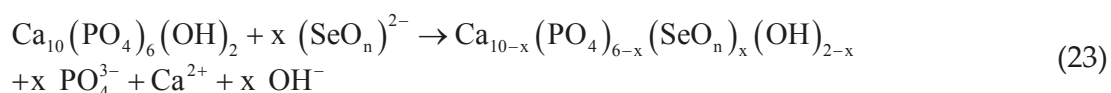
**Fig. 12.** Crystal structure of Sr<sub>5</sub>(CrO<sub>4</sub>)<sub>3</sub>(Cu<sub>0.586</sub>O): (a) projection along the c-axis and (b) side view showing the infinite [CuO]<sup>-</sup> chains and the coordination polyhedra of Cr and Sr atoms [76].

This phase crystallizes in the space group  $P6_3/M$  with hexagonal unit cell parameters:  $a = 10.0292 \text{ \AA}$  and  $c = 7.4623 \text{ \AA}$ ,  $V = 650.033 \text{ \AA}^3$  and  $Z = 2$ . The compound is stable up to  $1200^\circ\text{C}$  in air. It was found that copper in the form of  $\text{Cu}^+$  cations is located in infinite linear  $(\text{CuO})^-$  chains inserted into the tunnels parallel to hexagonal  $c$ -axis. The chains contain about 40% vacancies in copper positions. The valence states of Cr and Cu may be mainly +5 and +1, respectively [76].

#### 6.2.4. Selenium analogues of apatite

Selenium oxyanion-substituted hydroxyapatite (SeHAP) was synthesized as a promising material for the treatment of bone cancer to reduce the probability of recurrence, because selenium plays an important role in protein functions and it has significant effect on the induction of cancer cell apoptosis [77]. Another study indicated that selenite ( $\text{SeO}_3^{2-}$ ) or selenate ( $\text{SeO}_4^{2-}$ ) oxyanions exert their cancer chemopreventive effects by direct oxidation of critical thiol-containing cellular substrates and that they are more efficacious anticarcinogenic agents than selenomethionine or selenomethylselenocysteine with a lack of oxidation capability [3],[78].

Selenium was incorporated into the hydroxyapatite lattice by replacing some of the phosphate groups with selenite groups.  $\text{SeO}_4^{2-}$  (selenate) ion has tetrahedral structure like  $\text{PO}_4^{3-}$  ion (**Fig. 5** and **Table 4** in **Section 1.2**), but it is slightly larger ( $2.49 \text{ \AA}$ ) in diameter than phosphate ion, which is  $2.38 \text{ \AA}$  in diameter. By contrast,  $\text{SeO}_3^{2-}$  (selenite) ion has very similar diameter ( $2.39 \text{ \AA}$ ), but it has a quite different flat trigonal pyramid geometry. The substitution of bivalent selenium oxyanions forms positively charged vacancy compensated by simultaneous decalcification and dehydroxylation according to the reaction [3],[79]:

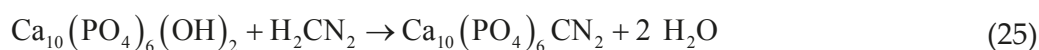


The SeHAP crystal lattice parameters increased slightly as the Se concentration increased when the Se/P ratios were less than 0.5 [80]. All samples prepared via the precipitation method from aqueous solution by KOLMAS et al [79] contained significant amount of carbonates, especially of B-type. Thus, for these samples, the formula  $\text{Ca}_{10-x}(\text{PO}_4)_{6-x}(\text{SeO}_n)_x(\text{OH})_{2-x}$  (**Eq. 23**) should be written as  $\text{Ca}_{10-x-y}(\text{PO}_4)_{6-x-y}(\text{SeO}_n)_x(\text{CO}_3)_y(\text{OH})_{2-x-y}$ . Hydroxyapatites containing selenate ions are non-toxic, whereas hydroxyapatite with the highest concentration of selenites is toxic.

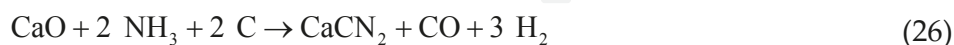
### 6.3. Substitution at Z-site

#### 6.3.1. Nitrogen-containing apatites

Nitrogen was incorporated into hydroxyapatite by dry ammonia treatments at temperatures between  $900$  and  $1200^\circ\text{C}$  in the presence of graphite. The process of synthesis of cyanamidapatite ( $\text{Ca}_{10}(\text{PO}_4)_6\text{CN}_2$ ,  $\text{Ca}_{10}(\text{PO}_4)_6\text{NCN}$ ) can be described by the following chemical equations [13]:

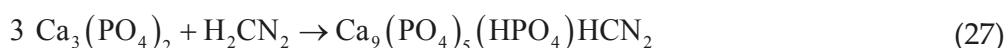


Ammonia reacts with graphite during the thermal treatment forming  $[\text{CN}_2]^{2-}$  ions (Eq. 24). These cyanamide ions interchange with moveable  $\text{OH}^-$  ions situated on the sixfold screw axis of apatite to form cyanamidapatite (Eq. 25). A similar reaction is known for the synthesis of calcium cyanamide from calcium oxide:



The treatments at temperatures above  $1200^\circ\text{C}$  or long-term treatments destroy the apatite lattice completely through the phosphate reduction. Cyanimide ions lose their sites in the apatite lattice and the nitrogen content decreases [13]. The synthesis of  $\text{Ca}_{10}(\text{PO}_4)_6\text{CN}_2$  apatite provides the evidence that the hydroxylapatite structure is able to incorporate larger organic molecules [81].

Direct transformation of TCP ( $\text{Ca}_3(\text{PO}_4)_2$ ) into cyanamidapatite according to the reaction:



was also proposed by HABELITZ et al [82].

### 6.3.2. Peroxide-doped apatites

Although “oxygenated” apatites were not much investigated compared to other substituted apatites, some past studies have, however, reported the possibility of apatitic channels to incorporate oxygenated species such as  $\text{H}_2\text{O}_2$  or  $\text{O}_2$  or molecular ions including  $\text{O}_2^{2-}$  (the peroxide ion) and superoxide  $\text{O}_2^-$ . They are single-phase nanocrystalline apatites, where part of apatitic  $\text{OH}^-$  ions are replaced by oxygenated species. Typically by peroxide ions (quantified) and at least the traces of superoxide ions can be prepared by the precipitation from aqueous calcium and phosphate solutions in the presence of  $\text{H}_2\text{O}_2$  under medium room temperature [83],[84].

The local structure of hydroxyl-peroxy apatite was described by YU et al [85]. Hydroxyl-peroxy apatite contains a small amount of partially dehydroxylated hydroxyapatite phase and calcium hydroxide. The incorporation of peroxide ions into the lattice of HAP causes the perturbations of hydrogen environments and slight changes in its crystal morphology. The distance between H in some structural  $\text{OH}^-$  and adjacent O along the c-axis becomes longer instead of forming the hydrogen bond after the incorporation of peroxide ions.

According to the concentration of peroxide ions in hydroxyl-peroxy apatite and the theoretical value, the corresponding formula for the hydroxyl-peroxy apatite is proposed as follows [85]:

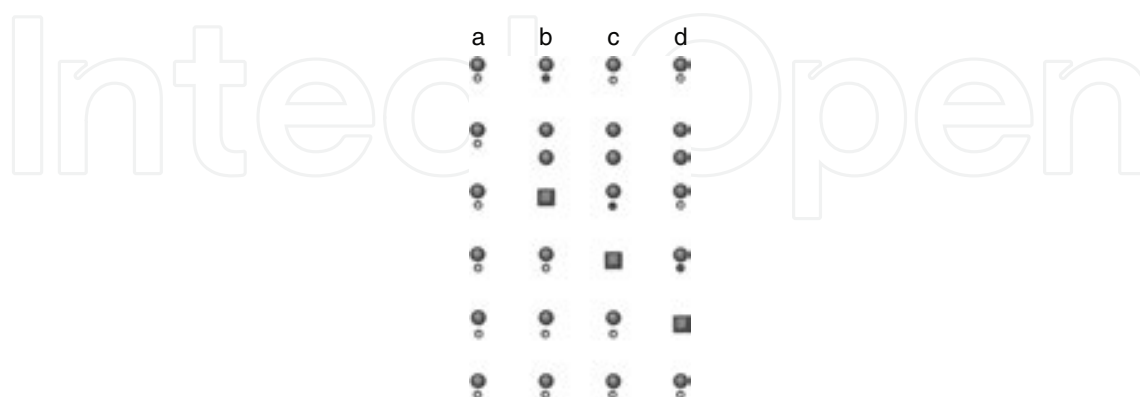
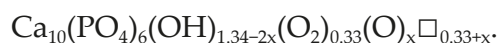


**Fig. 13.** Possible configuration of hydroxyl ions, peroxide or oxide ions and vacancies in the channel along the crystallographic c-axis in hydroxyl-peroxy apatite. O, H atoms and vacancies are presented by large gray circles, small open circles and gray squares, respectively. Filled small circles represent H atoms perturbed by the incorporation of peroxide ions [85].

A scheme of possible configurations of hydroxyl ions, peroxide or oxide ions and vacancies in the channel along the crystallographic c-axis in hydroxyl-peroxy apatite is illustrated in **Fig. 13**. Peroxide ions incorporated into HAP are located in the channel of apatite structure through the substitution of a portion of  $\text{OH}^-$  radicals, and the material is a solid solution of hydroxyl- and peroxide apatite.

ZHAO et al [86] reported that a new hydrogen bond was formed between peroxide ions and adjacent  $\text{OH}^-$  radicals in hydroxyl-peroxy apatite. According to the literature [430,446], the formation of hydrogen bond would induce a downfield shift of corresponding proton resonance. Some authors reported a linear correlation of the isotopic proton chemical shift with the  $\text{O-H}\cdots\text{O}$  distance, which was a measure of the hydrogen bond strength. ZHAO et al [86] suggested the following mechanism for the incorporation of  $\text{O}_2^{2-}$ :



where  $[\Box]$  was the vacancy.  $\text{O}^{2-}$  ion was active and could react with  $\text{O}_2$  to produce  $\text{O}_2^{2-}$ .



Peroxide ions associated with the vacancies were situated placed in the channel of HA lattice along the c-axis through the substitution of a portion of OH radicals. The molecular ions

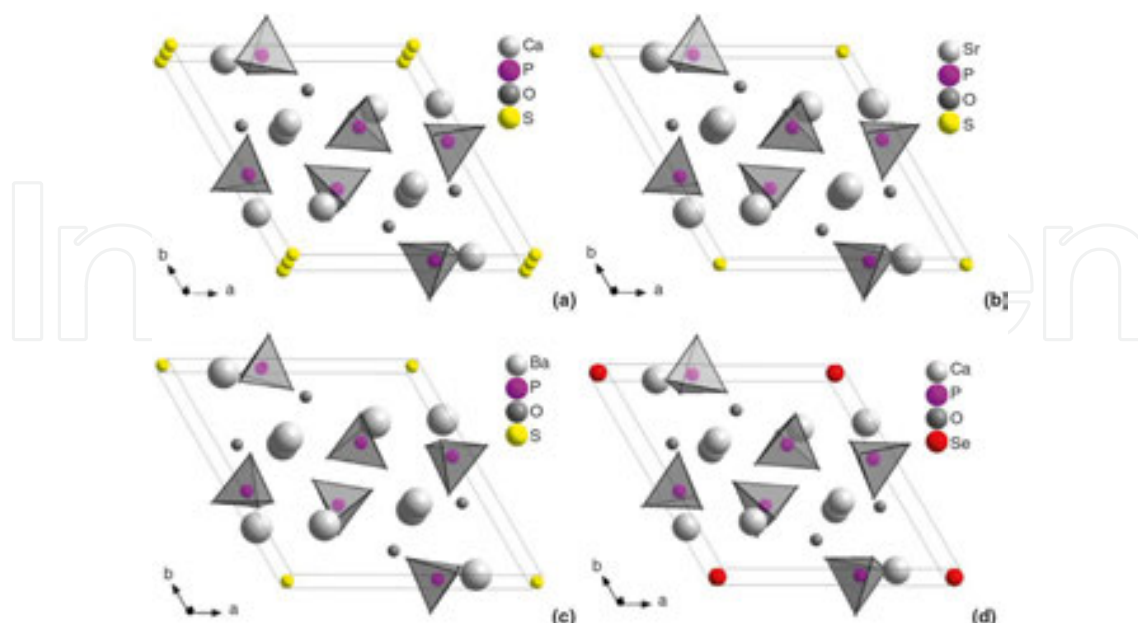
constituted a symmetric vibrator with a stretching vibration active in Raman spectrometry. This vibration was recorded at  $750\text{ cm}^{-1}$  in the Raman spectra of  $\text{O}_2^{2-}$ -containing HA samples. The final product was a solid solution of hydroxyl- and peroxide-apatite. However, the existence of peroxide ions in the HA lattice caused the contraction of the unit-cell dimensions of HA materials. In addition, a new hydrogen bond was formed between peroxide ions and adjacent OH radicals, which was determined by using molecular spectroscopy analysis. During annealing treatment in air, peroxide ions decomposed and the substituted OH radicals re-entered the HA lattice, resulting in the elimination of the structural aberrations caused by the incorporation of peroxide ions. The concentration of peroxide ions present in HA samples was measured by chemical analysis [86].

### 6.3.3. Chalcogenide phosphate apatites

The synthesis and the structure of four new chalcogenide<sup>5</sup> [87] phosphate apatitic phases of the composition given by the formula:

1.  $\text{Ca}_{10}(\text{PO}_4)_6\text{S}$ :  $a = 9.4619\text{ \AA}$ ,  $c = 9.8342\text{ \AA}$ ,  $c:a = 0.7223$  and  $V = 529.88\text{ \AA}^3$  (**Fig. 14(a)**);
2.  $\text{Sr}_{10}(\text{PO}_4)_6\text{S}$ :  $a = 9.8077\text{ \AA}$ ,  $c = 9.2089\text{ \AA}$ ,  $c:a = 0.7350$  and  $V = 600.53\text{ \AA}^3$  (**Fig. 14 (b)**);
3.  $\text{Ba}_{10}(\text{PO}_4)_6\text{S}$ :  $a = 10.2520\text{ \AA}$ ,  $c = 7.6590\text{ \AA}$ ,  $c:a = 0.7471$  and  $V = 697.14\text{ \AA}^3$  (**Fig. 14(c)**);
4.  $\text{Ca}_{10}(\text{PO}_4)_6\text{Se}$ :  $a = 9.5007\text{ \AA}$ ,  $c = 9.8406\text{ \AA}$ ,  $c:a = 0.7200$  and  $V = 534.73\text{ \AA}^3$  (**Fig. 14 (d)**).

were reported by HENNING et al [88].



<sup>5</sup> The elements from the chalcogenide group (or oxygen group family) belonging to Group 16 (VI A) of the periodic table: O, S, Se, Te and Po. Elements sulfur, selenium and tellurium are also termed as the elements from the sulfur subgroup [87].

**Fig. 14.** The structure of  $\text{Ca}(\text{PO}_4)_6\text{S}$  (a),  $\text{Sr}(\text{PO}_4)_6\text{S}$  (b),  $\text{Ba}(\text{PO}_4)_6\text{S}$  (c) and  $\text{Ca}(\text{PO}_4)_6\text{Se}$  (d) viewed along the c-axis.

These four apatites are isostructural and crystallize in the trigonal space group  $P3$  over bar with the chalcogenide ion positioned at  $(001/2)$ . Sulfoapatites show no ability to absorb  $\text{H}_2\text{S}$  in the way that oxyapatite absorbs  $\text{H}_2\text{O}$  at elevated temperatures. This can be attributed to the position of sulfide ion and the way it influences the crystal structure around vacant chalcogenide position at  $(000)$  [88].

### 6.3.4. Metaborate ion-containing apatite phase

Strontium borate-phosphate  $\text{Sr}_{10}(\text{PO}_4)_{5.5}(\text{BO}_4)_{0.5}(\text{BO}_2)^6$  was prepared from  $\text{SrCO}_3$ ,  $\text{NH}_4\text{H}_2\text{PO}_4$  and  $\text{H}_3\text{BO}_3$  at high temperature (from 1150 to 1550°C) and was found to be free of alkali metal compounds.  $\text{Sr}_{10}(\text{PO}_4)_{5.5}(\text{BO}_4)_{0.5}(\text{BO}_2)$  phase is a derivative of the apatite crystal structure with metaborate ion at Z-site: space group  $P3$ ,  $a = 9.7973 \text{ \AA}$ ,  $c = 7.3056 \text{ \AA}$ ,  $V = 607.29 \text{ \AA}^3$ ,  $Z = 1$  [89],[90], [91].

The strontium sites are found to be fully occupied, while  $[\text{PO}_4]^{3-}$  tetrahedra are partially replaced by  $[\text{BO}_4]^{5-}$  groups. The crystal structure contains Sr cations occupying the 6g (Sr(1)) and 2d (Sr(2), Sr(3)) sites, isolated tetrahedral  $[\text{PO}_4]^{3-}/[\text{BO}_4]^{5-}$  groups and linear  $[\text{BO}_2]^-$  groups located in hexagonally shaped (trigonal antiprismatic) channels formed by Sr(1) atoms and running along  $[001]$  (**Fig. 15**). The space group of the present compound is reduced to  $P3$ , because the orientation of the  $[\text{PO}_4]/[\text{BO}_4]$  tetrahedra destroys the mirror plane characteristic for the apatite crystal structure ( $P6_3/M$ ) [89],[91].

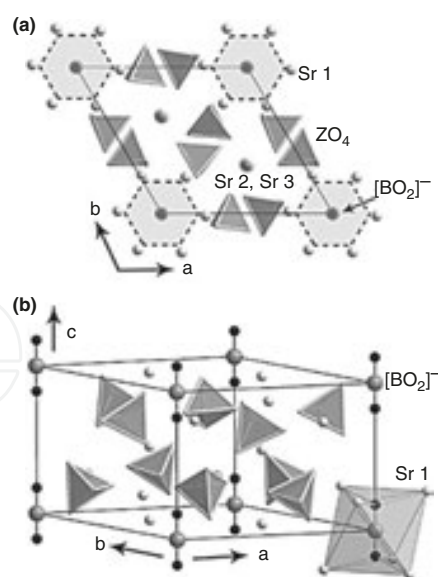


**Fig. 15.** Crystal structure of  $\text{Sr}_{10}(\text{PO}_4)_{5.5}(\text{BO}_4)_{0.5}(\text{BO}_2)$ : projection along  $[001]$  showing the hexagonally shaped channels formed by Sr(1) around the threefold inversion axis ( $Z = (P_{0.95}B_{0.05})$ ) (a) and side view emphasizing the linear  $[\text{BO}_2]^-$  groups and the corresponding trigonal antiprism formed by Sr(1) (b) [89].

<sup>6</sup> See also Section 5.3.



## 6.4. Solid solutions of apatites

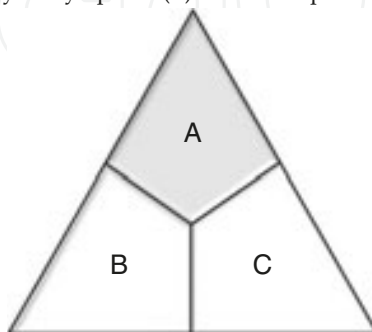
Crystalline solid solutions<sup>7</sup> [92] of apatites are frequently encountered where the possibility and type depend on the condition of formation or preparation, thermal history after formation and the end-members of the series [2]. The structure of ternary solid solution of hexagonal ( $P6_3/M$ ,  $Ca_5(PO_4)_3(F_{0.39}Cl_{0.33}OH_{0.28})$ ) and monoclinic ( $P2_1/B$ ,  $Ca_5(PO_4)_3(F_{0.29}Cl_{0.47}OH_{0.24})$ ) F-OH-Cl apatite was resolved by HUGHES et al [93]. Phosphate tetrahedra and Ca(l) polyhedra of both structures are generally very similar to analogous polyhedra in the end-member fluor-, chlor- and hydroxylapatite structures. Ca(2) polyhedron, which includes the column anions among its ligands, exhibits significant but regular variations in interatomic distances that can be directly correlated to Cl content.

The solid solution in hexagonal ternary apatite is achieved by a 0.4 Å shift along the c-axis of Cl atom relating to its position in end-member chlorapatite. This adjustment affects the Markovian sequence<sup>8</sup> [94] of anions in the (0,0,z) anion columns by providing a structural environment that includes column OH species at the distance of 2.96 Å from Cl. The shift of Cl atom is accompanied by splitting of Ca(2) atoms into two distinct positions as a function of the kind of anion neighbor (F or OH vs. Cl). Additional nonequivalent Cl site, similar to that in end-member chlorapatite, is also present. Those Cl atoms with adjacent OH occupy a site different from Cl atoms adjacent to vacancies in the anion column [93].

Reduction of symmetry in monoclinic ternary apatite results from the ordering of Cl and OH within the anion columns. The atomic positions of Cl and OH in the anion column are equivalent to those in hexagonal ternary apatite, but each is ordered into only one of the two hexagonal symmetry-equivalent sites [93].

The apatite supergroup minerals of the solid solution [95]:

<sup>7</sup> For the purposes of nomenclature, a complete solid-solution series without structural order of ions defining the end-members is arbitrarily divided at 50 mol.% ("50% rule") to two portions with different names. Analogously, the 50% rule applied to members of ternary solid-solution series implies that the mineral names should be given only to the three end-members. Each name should be applied to the compositional range from the end-member to the nearest right bisector of the sides of the composition triangle. For example, the apatite series  $Ca_5(PO_4)_3(F,OH,Cl)$  is represented by three compositional fields of fluorapatite (A), hydroxylapatite (B) and chlorapatite (C) [92].

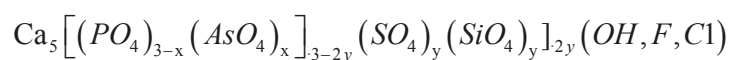


<sup>8</sup> Statistical model where a random sequence  $k$ , the probability distribution  $p(k)$  of which satisfies the equation [94]:

$$(a) \quad p(\bar{k}) = p(k_1) p(k_0^{i-1} | k_i) \quad p(k_{i+1}^n | k_i);$$

is referred to as the Markovian sequence or the Markovian chain.





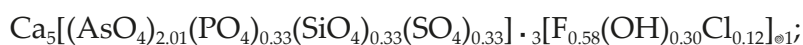
where  $x = 0 - 3$  and  $y = 0 - 1.5$  were found in altered calcareous xenoliths within the ignimbrite of the Upper Chegem caldera, Northern Caucasus, Russia. These minerals belonging to the apatite supergroup occur in all zones of skarn from the core to the contact with ignimbrite as follows: brucite-marble, spurrite ( $\text{Ca}_5(\text{SiO}_4)_2\text{CO}_3$  [96]), humite ( $\text{Mg}_7(\text{SiO}_4)_3(\text{F}, \text{OH})_2$  [97]) and larnite<sup>9</sup> ( $\text{Ca}_2\text{SiO}_4$  [98],[99],[100],[101]) zones. They are associated with both high-temperature minerals: reinhardbraunsite ( $\text{Ca}_5(\text{SiO}_4)_2(\text{OH})_2$  [102]), chegemite ( $\text{Ca}_7(\text{SiO}_4)_3(\text{OH})_2$  [103]), wadalite ( $\text{Ca}_6\text{Al}_5\text{Si}_2\text{O}_{16}\text{Cl}_3$  [104]), rondorfite ( $\text{Ca}_8\text{Mg}(\text{SiO}_4)_4\text{Cl}_2$  [105]), cuspidine ( $\text{Ca}_4(\text{Si}_2\text{O}_7)\text{F}_2$  [106]), lakargiite ( $\text{CaZrO}_3$  [107]) and srebrodolskite ( $\text{Ca}_2\text{Fe}^{3+}_2\text{O}_5$  [108]), corresponding to the sanidinite metamorphic facies,<sup>10</sup> and secondary low-temperature minerals: calcium hydrosilicates (hillebrandite [113], awfillite [114], bultfonteinite [115]), hydrogarnets [116] and minerals of the ettringite group [117].

The minerals of the apatite supergroup often form elongated cracked hexagonal or pseudo-hexagonal crystals up to 250  $\mu\text{m}$  in size as well as grain aggregates. A new solid-solution series was found between ellestadite and svabite-johnbaumite ( $\pm$ apatite) with the ellestadite type isomorphic substitution according the following scheme [95]:

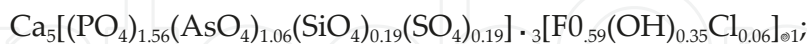


where  $R = \text{As}^{5+}$  and  $\text{P}^{5+}$ . The As content in investigated minerals decreases from the contact skarn zone with the ignimbrite towards the core of altered xenoliths (from 2.11 As pfu<sup>11</sup> to 0), for example [95]:

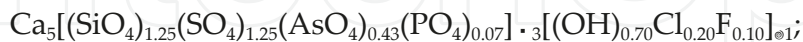
**i.** Svabite:



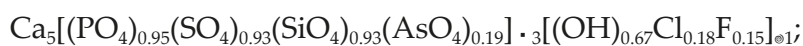
**ii.** As-bearing fluorapatite:



**iii.** As-bearing hydroxyllelestadite:



**iv.** Si, S-bearing hydroxylapatite:

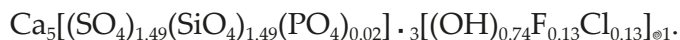


<sup>9</sup> The name is also often used for synthetic phase of the same composition (dicalcium silicate,  $\text{Ca}_2\text{SiO}_4$ ,  $\text{C}_2\text{S}$ ), which is the main component of belite in Portland cement [99],[100],[101].

<sup>10</sup> Since sanidinite facies are formed under conditions of intensive contact metamorphism at high temperatures and low pressure, volatiles such as carbon dioxide and water are removed from the rock. The components characteristic for the sanidinite facies are sanidine (feldspar,  $\text{KAlSi}_3\text{O}_8$  [109]), corundum (oxide,  $\text{Al}_2\text{O}_3$  [110]), cordierite (cyclosilicate,  $\text{Mg}_2\text{Al}_4\text{Si}_5\text{O}_{18}$  [111]), sillimanite (nesosilicate,  $\text{Al}_2\text{OSiO}_4$  [112]) and glass formed as the product of partial fusion.

<sup>11</sup> The abbreviation for per formula unit (pfu), see also **Footnote 36** in **Chapter 1**.

## v. Hydroxyllelestadite:



The crystals of As-bearing phases belonging to the investigated solid solution are heterogeneous and small in size. Therefore, X-ray single-crystal data were obtained for only Si, S, As-bearing hydroxylapatite (see the formula above):  $P6_3/M$ ,  $a = 9.5193 \text{ \AA}$ ,  $c = 6.9052 \text{ \AA}$ ,  $V = 541.90 \text{ \AA}^3$  and  $Z = 4$ . The Raman spectroscopy also confirms that the investigated samples belong to the arsenate phosphate-silicate-sulfate multiple solid solution [95].

The hydrothermal synthesis of vanadate/phosphate hydroxyapatite solid solutions of the composition of  $\text{Ca}_{10}(\text{VO}_4)_x(\text{PO}_4)_{6-x}(\text{OH})_2$ , where  $x = 0, 1, 2, 3, 4, 5$  and  $6$ , was firstly reported by ONDA et al [118]. The lattice parameters increased linearly with increasing content of vanadium according to Vegard's law. The apatite crystals were precipitated in the form of column crystals with the length of about 40 – 100 nm and the width of about 25 – 40 nm. The sizes of the nanoparticle solid solutions increased with increasing vanadium content, whereas the morphology was independent of the vanadate/phosphate ratio. Calcium hydroxyapatites substituted with vanadate were also prepared by SUGIYAMA et al [119] and used as catalysts in oxidative dehydrogenation of propane. The catalytic activity<sup>12</sup> of vanadate-substituted calcium hydroxyapatites was evidently greater than that of magnesium pyrovanadate, which is one of the most active catalysts for this oxidation.

The crystal structure of 11 samples of synthetic Na-Ca-sulfate apatite systems of the composition of  $\text{Na}_{6.45}\text{Ca}_{3.55}(\text{SO}_4)_6(\text{F}_x\text{Cl}_{1-x})_{1.55}$ , where  $x = 0 - 1$ , was refined by PIOTROWSKI et al [120] in the  $P6_3/M$  space group ( $Z = 1$ ). The sulfate tetrahedra and the two symmetrically independent cation polyhedra around M(1) and M(2) (occupied by Na and Ca, respectively) are generally very similar to analogous polyhedra in phosphate apatites. A common structural feature of all members of the solid-solution series is the deficiency in total  $\text{Cl}^-$  and  $\text{F}^-$  content compared to phosphate apatites. The mean value of  $(\text{Cl} + \text{F})$  for the solid solution equals 1.55(6) atoms per unit cell compared to the ideal value of 2 atoms per unit cell observed in phosphate apatites. The solid-solution series  $\text{Na}_{6.45}\text{Ca}_{3.55}(\text{SO}_4)_6\text{Cl}_{1.55} + \text{Na}_{6.45}\text{Ca}_{3.55}(\text{SO}_4)_6\text{F}_{1.55}$  shows a gap towards the side of fluoride-rich compounds. Under ambient pressure, the gap exists between  $0 < n_{\text{Cl}}/n_{\text{Cl}} + n_{\text{F}} < 0.33$ , where  $n_{\text{Cl}}$  and  $n_{\text{F}}$  represent the numbers of  $\text{Cl}^-$  and  $\text{F}^-$  atoms per unit cell, respectively.

Lead apatites form a family of isomorphous compounds, and well-known members of the group are mimetite ( $\text{Pb}_5(\text{AsO}_4)_3\text{Cl}$ , **Section 1.6.7**) and pyromorphite ( $\text{Pb}_5(\text{PO}_4)_3\text{Cl}$ , **Section 1.6.4**). Isostructural with vanadinite  $\text{Pb}_5(\text{VO}_4)_3\text{Cl}$ , these three constituents form a ternary system within the apatite group of  $P6_3/M$  symmetry (hexagonal bipyramid). The mimetite and pyromorphite structures can incorporate numerous admixtures, mainly Ca, Ba, As, V, P and others. The most common substitution is the isovalent replacement of part of Pb with Ca and As with P and V. Extensive substitution of  $(\text{AsO}_4)^{3-}$  group by tetrahedrally coordinated and isovalent  $(\text{PO}_4)^{3-}$  ion is well established by the existence of a complete solid solution between mimetite and pyromorphite [121].

<sup>12</sup> The utilization of apatites as catalysts is described in **Section 10.7**.

A number of compounds of the mimetite  $\text{Pb}_5(\text{AsO}_4)_3\text{Cl}$ -pyromorphite  $\text{Pb}_5(\text{PO}_4)_3\text{Cl}$  solid-solution series were synthesized at room temperature by BAJDA et al [121] and investigated with Raman and infrared spectroscopy. The peak positions of the dominant antisymmetric stretching ( $\nu_3$ ) and bending ( $\nu_4$ ) vibrations in the  $720 - 1040 \text{ cm}^{-1}$  and  $400 - 580 \text{ cm}^{-1}$  regions of the Raman and IR spectra of minerals from the mimetite-pyromorphite series vary primarily as a function of the As/(As + P) ratio in the solids' structure. It is due to the effect of the atomic mass and bond forces on the banding energies of the substituting tetrahedra. The observed correlation between the band positions and the extent of the anionic substitution among the series can be used to estimate the As and P content in mimetite-pyromorphite solid solutions [121].

Solid solutions of  $\text{Pb}_8\text{M}_2(\text{XO}_4)_6$  lead alkali apatites were studied by MAYER et al [122]. The  $\text{Pb}_8\text{Na}_{2-x}\text{K}_x(\text{PO}_4)_6$ ,  $\text{Pb}_8\text{Na}_{2-x}\text{K}_x(\text{AsO}_4)_6$ ,  $\text{Pb}_8\text{Na}_{2-x}\text{Rb}_x(\text{PO}_4)_6$  and  $\text{Pb}_8\text{K}_{2-x}\text{Rb}_x(\text{PO}_4)_6$  compounds crystallize at all compositions in the  $\text{P6}_3/\text{M}$  hexagonal apatite structure and form true solid solutions.

Some other examples of apatite solid solutions are listed below [2]:

- $\text{Ca}_2\text{Y}_8(\text{SiO}_4)_6\text{O}_2 - \text{Ca}_8\text{Y}_2(\text{PO}_4)_6\text{O}_2$ ;
- $\text{Ca}_2\text{La}_8(\text{SiO}_4)_6\text{O}_2 - \text{Ca}_8\text{La}_2(\text{PO}_4)_6\text{O}_2$ ;
- $\text{Ca}_2\text{Y}_8(\text{SiO}_4)_6\text{O}_2 - \text{Y}_{10}(\text{SiO}_4)_4(\text{BO}_4)_2\text{O}_2$ ;
- $\text{Mg}_2\text{Y}_8(\text{SiO}_4)_6\text{O}_2 - \text{Y}_{10}(\text{SiO}_4)_4(\text{BO}_4)_2\text{O}_2$ ;
- $\text{Pb}^{4+}_3\text{Pb}^{2+}_5\text{Y}_2(\text{SiO}_4)_6\text{O}_2 - \text{Pb}^{2+}_2\text{Y}_8(\text{SiO}_4)_6\text{O}_2$ ;
- $\text{Ca}_{10}(\text{PO}_4)_6(\text{OH})_2 - \text{Ca}_4\text{Y}_6(\text{SiO}_4)_6(\text{OH})_2$ ;
- $\text{M}_{10}(\text{PO}_4)_6\text{F}_2 - \text{M}_{10}(\text{PO}_4)_6\text{F}_2$  ( $\text{M} = \text{Sr}, \text{Ba}, \text{Pb}$ );
- $\text{M}_{10}(\text{PO}_4)_6\text{F}_2 - \text{M}_{10}(\text{MnO}_4)_6\text{F}_2$  ( $\text{M} = \text{Sr}, \text{Ba}, \text{Pb}$ ).

## 6.5. Trace elements and their isotopes

Since apatite is an important accessory mineral in most common rock types, it is often used in trace element and isotope investigations of igneous and metamorphic rocks [123]. Stable isotope compositions of biologically precipitated apatite in bone, teeth and scales are widely used to obtain the information on the diet, behavior and physiology of extinct organisms and to reconstruct past climate in terrestrial and marine conditions [124].

Broad spectrum of substitutions in the apatite lattice allows the incorporation of various isotopes, which offer a number of instruments for the interpretation of paleoenvironment and diagenesis. The relative stability of francolite compared to other sedimentary minerals led to an enormous number of studies and applications. Various isotopes occupy the  $\text{Ca}^{2+}$  and  $\text{PO}_4^{3-}$  sites in the lattice of apatite (Fig. 16).

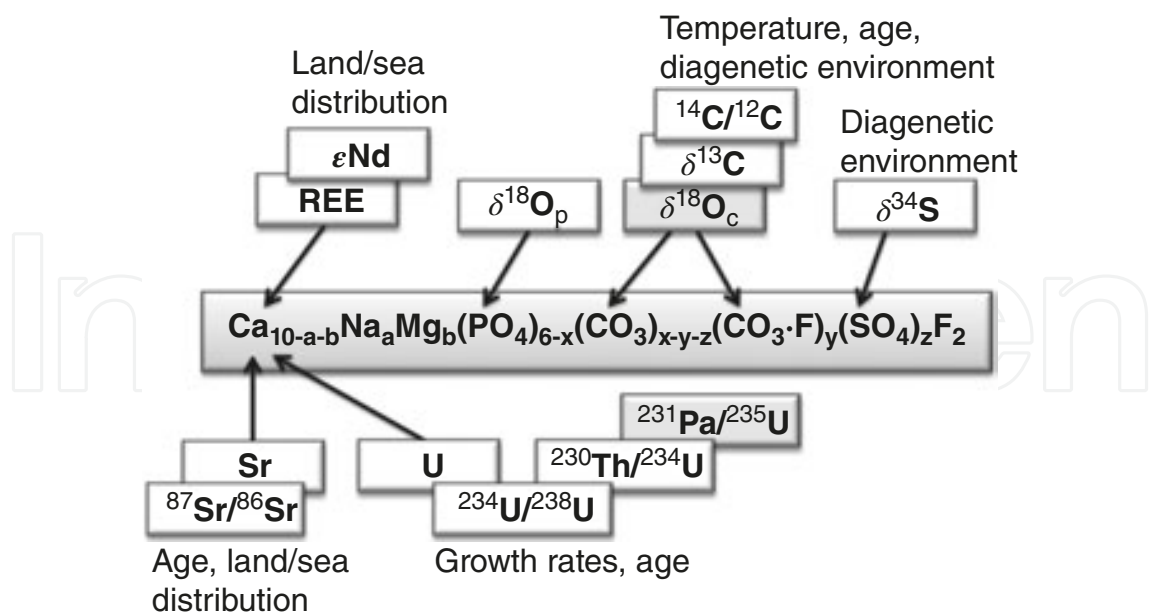


Fig. 16. Possible isotopic substitutions in the structure of francolite [125].

Since the earliest application in deep-time study of Late Cretaceous paleotemperatures in 1950, the oxygen isotope paleothermometry is based on the temperature dependence of oxygen isotope fractionation between authigenic minerals<sup>13</sup> [126] and ambient waters. Under the equilibrium conditions, the  $^{18}\text{O}/^{16}\text{O}$  ratio of sedimentary carbonate and phosphate minerals depends only on the temperature of precipitation and on the  $^{18}\text{O}/^{16}\text{O}$  ratio of ambient water. Thermodynamic relationships and bond vibrational frequencies can be used to determine the mineral-water isotopic fractionation relations but not with the precision and accuracy necessary for the paleothermometry. Such an application requires the calibrations based on mineral-water oxygen exchange experiments at high temperatures, mineral precipitation experiments at low temperatures and/or natural experiments using minerals grown under known conditions [127],[128].

Carbon, oxygen and sulfur isotopes are used to reconstruct the oxygenation stages of the sediments during organic matter degradation and precipitation of apatite. The application of this method gives good results for modern and Neogene deposits. In older occurrences, the signature of carbon and oxygen composition is commonly overprinted by diagenetic and burial diagenesis [125],[129]. The carbon isotope ratios of apatite can be used to interpret the source of carbon in magmas and metamorphic fluids using the assumption that the carbon isotope fractionations between phases are small in igneous and metamorphic systems [123].

The carbon isotope analysis of bioapatites was first applied to terrestrial mammals in early 1980s [130],[131],[132]. While it is now known that some bones do undergo the C-isotope exchange extremely readily, collagen, bone and enamel record different periods of time during

<sup>13</sup> The minerals of sedimentary rocks are subdivided into two main groups [126]: authigenic (formed on their present position) and allogenic (transported to its current position from elsewhere). Both groups will be further described in Chapter 7.

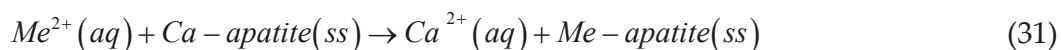
the life of a single individual, and the diet may change. That means, there is a fundamental ambiguity (preservation vs. normal intraindividual differences) in interpreting the isotopic differences among different tissues. Unfortunately, early results were taken to imply that all bioapatites are unreliable, and it was not until the 1990s that it became accepted that the tooth enamel, at least, is a robust recorder of diet. Thus, the early work of LEE-THORP and VAN DER MERWE [133],[134] was a struggle against the tide of misplaced opinions [129].

Fossil biogenic apatites display the trace element compositions that can record environmental and biological signals, give insights into past water compositions or be used for dating paleontological and archeological bones and teeth. The mechanisms of the process of trace element and their isotopes incorporation into apatites of skeletal phosphatic tissues are described by REYNARD and BALTER [135]:

1. Partitioning between aqueous fluids and crystals;
2. Surface adsorption, complexation and chelation;
3. Diffusion processes.

#### 6.5.1. Partitioning of divalent cations

Partitioning of divalent cations is defined by the chemical equilibrium expressing the divalent cation ( $\text{Me}^{2+}$ ) exchange between apatite and aqueous solutions [135]:



where (aq) and (ss) refer to the aqueous solution and to the solid solution, respectively. The equilibrium constant of Eq. 31 can be written as

$$K_D \left( \frac{\text{Me}^{2+}}{\text{Ca}} \right) = \frac{\frac{x_{\text{Me-apatite}}}{x_{\text{Ca-apatite}}}}{\frac{m_{\text{Me}^{2+}}}{m_{\text{Ca}^{2+}}}} = \frac{\frac{K(T)_{\text{Ca-apatite}}}{K(T)_{\text{Me-apatite}}} \frac{\lambda_{\text{Ca-apatite}}}{\lambda_{\text{Me-apatite}}} \frac{\gamma_{\text{Me}^{2+}}}{\gamma_{\text{Ca}^{2+}}}}{\quad} \quad (32)$$

where  $x$  is the molar fraction in apatite solid solution,  $m$  is the molality in water,  $\lambda$  is the activity coefficient of the component in the solid solution,  $K(T)$  is the solubility product of the end-member at temperature  $T$  and  $\gamma$  is the ion activity in the aqueous solution, the ratio of which in water is assumed to be equal to one. The activity coefficients in regular solid-solution model are described by Margules parameters<sup>14</sup> [136] and can be approximated by the elastic energy due to the deformation of the host crystal lattice around the substituted cation [135],[137]:



$$W_{G_{ij}} = 4\pi N_A E \left[ \frac{r_i}{2} (r_j - r_i)^2 + \frac{1}{3} (r_j - r_i)^3 \right] \quad (33)$$

where  $N_A$  is the Avogadro number,  $E$  is the Young's modulus of the crystal,  $r_i$  is the ionic radius of cation normally occupying the site in the  $i$ -compound (Ca in apatite) and  $r_j$  is the ionic radius of the substituted cation in compound  $j$ . The elasticity of hydroxyapatite gives  $E = 114 \pm 2$  GPa.

At low concentrations ( $X_{\text{Me-apatite}} \ll 1$ ) like those of trace elements in biogenic apatites, **Eq. 32** is reduced to the relationships [135]:

$$K_D \left( \frac{\text{Me}^{2+}}{\text{Ca}} \right) = \frac{K(T)_{\text{Ca-apatite}}}{K(T)_{\text{Me-apatite}}} \exp \left( \frac{-W_{\text{MeCa}}}{RT} \right) = \exp \left( -\frac{G_{\text{ideal}} + W_{\text{MeCa}}}{RT} \right) \quad (34)$$

where the term  $\exp(-\Delta G_{\text{ideal}}/RT)$  is the free enthalpy change of the **reaction 31**, equivalent to the ratio of end-member solubility products. Unlike carbonates, the data of solubility products and thermodynamics for end-member apatites are scarce. When no data are available for the solubility and enthalpy of formation of the end-members, it is assumed that the elastic energy term dominates over the partitioning, i.e.  $\Delta G_{\text{ideal}} \ll W_{\text{MeCa}}$ . Promising ways for obtaining the enthalpies of formation and the substitution energies are the first-principle calculations [138] and the atomistic modeling [135],[139].

For heterovalent substitutions, the equilibrium reaction becomes complex since complementary substitutions are necessary to maintain the charge balance in the crystal. Typically, the substitution of trivalent elements of important rare-earth series requires the compensation by  $\text{Na}^+$  for  $\text{Ca}^{2+}$  at an adjacent site or even more complex substitution scheme involving carbonate groups or fluorine. In that case, most thermodynamic data required for the calculation of the equilibrium constant are not available. Among the series of elements with the same charge and substitution scheme, the pattern of equilibrium constants, or of distribution coefficients, can be approximated by combining **Eqs. 33 and 34** [135]:

<sup>14</sup> The Margules equation expresses the Gibbs free energy ( $G^E$ ) of binary liquid mixture ( $x_1 + x_2 = 1$ ) in the symmetric form [136]:

$\frac{G^E}{RT} = A_1 x_1 + A_2 x_2$ ; where  $A_1 = A + B$  and  $A_2 = A - B$ . Applying the partial molar derivative produces the expression for the activity coefficients:

$$\ln \gamma_1 = x_2^2 [A_2 + 2x_1 (A_1 - A_2)] \text{ and } \ln \gamma_2 = x_1^2 [A_1 + 2x_2 (A_2 - A_1)].$$

The Margules expressions for activity coefficients are based on the Lewis-Randall standard state (pure substance in the same phase and the same temperature and pressure as the mixture); therefore, they must obey the pure-component limit ( $\lim_{x_i \rightarrow 1} \gamma_i = 1$ ). The parameters  $A_1$  and  $A_2$  are simply related to the activity coefficients at infinite dilution:  $\lim_{x_1 \rightarrow 0} \gamma_1^\infty = A_1$

and  $\lim_{x_2 \rightarrow 0} \gamma_2^\infty = A_2$ . For the binary mixture, where  $\gamma_1^\infty = \gamma_2^\infty \Rightarrow A_1 = A_2$ , the Margules equation collapses to Porter equation. The multicomponent version of the Margules equation is [136]:

$$\frac{G^E}{RT} = \sum \sum_{i < j} x_i x_j [A_{ij} + B_{ij} (x_i - x_j)].$$

$$K_D = K_D^0 \exp \left( -4\pi N_A E_{\text{eff}} \left[ \frac{r_0}{2} (r_j - r_0)^2 + \frac{1}{3} (r_j - r_0)^3 \right] / RT \right) \quad (35)$$

where  $E_{\text{eff}}$  is the effective Young's modulus and  $r_0$  is the optimum radius for maximum equilibrium constant  $K_D^0$ , all of which will depend on the charge of the considered series of elements. These parameters can be adjusted to experimental data such as partition coefficients between minerals and liquids and lead to parabola-like curves, the position and curvature of which depend on the charge of the element. This approach was applied so far only to rare-earth elements in apatite, where the relative partition coefficients were extrapolated from magmatic temperatures around 800°C to low temperatures appropriate for fossil diagenesis [135].

### 6.5.2. Complexation of metal cations

The complexation of metal cations in aqueous fluids involves binding with a broad range of molecules from simple inorganic ones (e.g. carbonates, phosphates and sulfates) to complex organic ones (humic acids, amino acids, proteins, enzymes, etc.). For molecules with several bonding sites and structural flexibility (e.g. multidentate or chelator), the complexation is thermodynamically favored with respect to the complexation with several monodentates having one bonding site; the process is named chelation. Chelators can be adsorbed on mineral surfaces while remaining complexed to metallic cations. The pattern of the partition coefficients associated with this process was measured for rare-earth elements complexed with humic acids and manganese oxides. It shows null fractionation along the whole series; the effect of chelation is therefore to screen the trace element in the crystal or ligand field and to suppress the fractionation associated with ionic radius variations and tetrad effects, and most of the anomalies associated with redox of Ce [140]. Similar effects might occur for the adsorption of chelated metals on other mineral surfaces and in particular phosphates. In addition to chelators, the transition metals also form complexes with proteins and enzymes that interact with bones and teeth in living organisms and may influence their incorporation in bioapatite [135].

### 6.5.3. Diffusion processes

Solid-state diffusion in crystals is a thermally activated process governed by the enthalpy of formation and of migration of defects and usually well described by the Arrhenius relation [135]:

$$D = D_0 \exp \left( -\frac{\Delta H_a}{RT} \right) \quad (36)$$

where  $D_0$  is the pre-exponential factor corresponding to the diffusion coefficient at infinite temperature and  $\Delta H_a$  is the activation enthalpy (or energy) of the diffusion process. The



extrapolation of high-temperature diffusion data of trace elements in apatite shows that these processes are inefficient at temperatures below 300°C, which cover the conditions of diagenetic alteration up to low-grade metamorphism [135],[141].

The differing initial and boundary conditions imposed in three sets of diffusion experiments:

1. Ion implantation;
2. In-diffusion with powder sources experiment;
3. Out-diffusion.

consequently resulting in different solutions to the diffusion equation. However, in all cases, the process can be described as one-dimensional, concentration-independent diffusion [141].

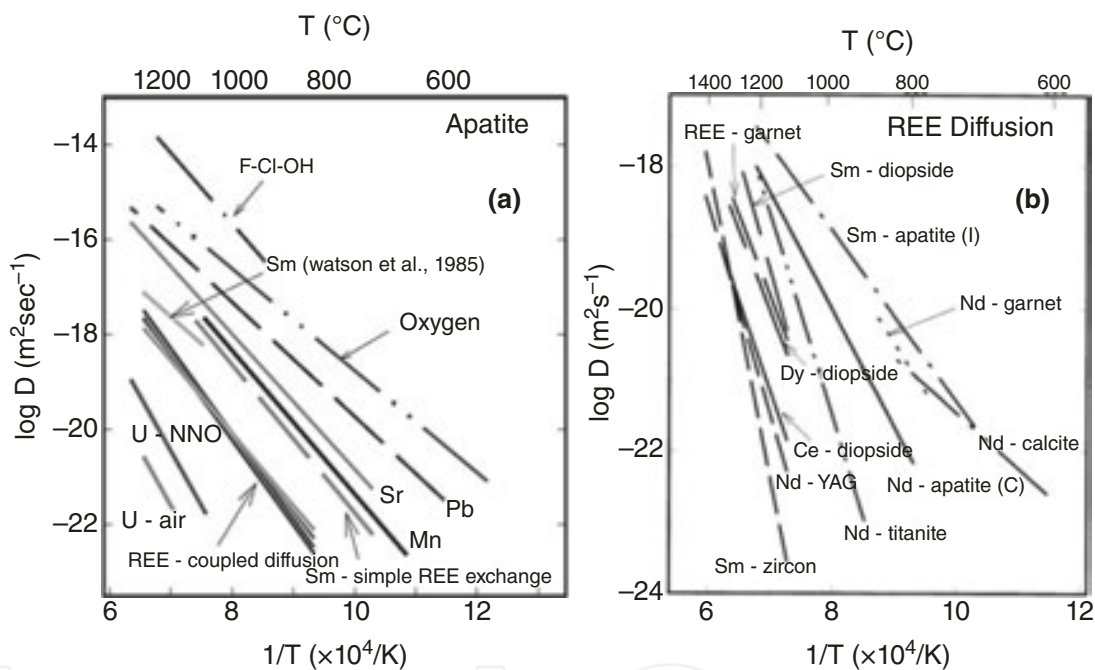


**Fig. 17.** The summary of data diffusion for cations and anions in apatite (a) [142] and the diffusion of Sm and Nd for various minerals and oxides (a) [141].

A plot of diffusivities of various cations and anions in apatite is shown in **Fig. 17(a)**. The diffusivities of Mn are similar to those of Sr and about an order of magnitude slower than those of Pb. On the other hand, the diffusion of  $\text{Mn}^{2+}$  in apatite is about two orders of magnitude faster than the diffusion of (trivalent) REE when coupled substitutions according to **Eqs. 4** and **5** are involved [141],[142]. The diffusion coefficients of Nd and Sm in various minerals and related oxides are plotted in **Fig. 17(b)**. The diffusion of REE in apatite is relatively fast; when only simple REE exchange is involved, it is among the fastest in rock-forming minerals for which the data exist. Even when the chemical diffusion involving coupled exchange is considered, REE transport in apatite is considerably faster than the REE diffusion in other accessory minerals [141].

## Author details

Petr Ptáček

Brno University of Technology, Czech Republic

## References

- [1] Valsami-Jones E. Phosphorus in Environmental Technologies: Principles and Applications: Principles and Applications (Integrated Environmental Technology). 1st ed., London: IWA Publishing, 2004. ISBN 1-84339-001-9
- [2] Alper A. Phase Diagrams 6-V: Materials Science and Technology. Elsevier, 2012. ISBN 978-0323154895
- [3] Šupová M. Substituted hydroxyapatites for biomedical applications: A review. *Ceramics International* 2015;41(8) 9203–9231.
- [4] Cox SC, Jamshidi P, Grover LM, Mallick KK. Preparation and characterisation of nanophase Sr, Mg, and Zn substituted hydroxyapatite by aqueous precipitation. *Materials Science and Engineering: C* 2014;35 106–114.
- [5] Iafisco M, Ruffini A, Adamiano A, Sprio S, Tampieri A. Biomimetic magnesium–carbonate-apatite nanocrystals endowed with strontium ions as anti-osteoporotic trigger. *Materials Science and Engineering: C* 2014;35 212–219.
- [6] Landi E, Tampieri A, Mattioli-Belmonte M, Celotti G, Sandri M, Gigante A, Fava P, Biagini G. Biomimetic Mg- and Mg,CO<sub>3</sub>-substituted hydroxyapatites: synthesis characterization and in vitro behavior. *Journal of the European Ceramic Society* 2006;26(13) 2593–2601.
- [7] Tamm T, Peld M. Computational study of cation substitutions in apatite. *Journal of Solid State Chemistry* 2006;179(5) 1581–1587.
- [8] Cockbain AG. The crystal chemistry of the apatites. *Mineralogical Magazine* 1968;36(281) 654–660.
- [9] Cockbain AG, Smith GV. Alkaline-earth-rare-earth silicate and germanate apatites. *Mineralogical Magazine*, 1967;36 411–421.
- [10] Nickel EH, Grice JD. The IMA commission on new minerals and mineral names: procedures and guidelines on mineral nomenclature. *Canadian Mineralogist* 1998;36 3–16.
- [11] Levinson AA. A system of nomenclature for rare-earth minerals. *American Mineralogist* 1966;51 152–158.

- [12] Brown PW, Constanz B. Hydroxyapatite and Related Materials. CRC Press, 1994. ISBN: 978-0849347504
- [13] Habelitz S, Pascual L, Durán A. Nitrogen-containing apatite. *Journal of the European Ceramic Society* 1999;19(15) 2685–2694.
- [14] Ding T, Ma D, Lu J, Zhang R. Apatite in granitoids related to polymetallic mineral deposits in southeastern Hunan Province, Shi-Hang zone, China: Implications for petrogenesis and metallogenesis. *Ore Geology Reviews* 2015;69 104–117.
- [15] Deer WA. Rock-forming minerals: Non-silicates, volume 5B, second edition. Geological Society of London, 1998. ISBN: 978-1897799901
- [16] Hewlett P. Lea's Chemistry of Cement and Concrete. 4th ed., Butterworth-Heinemann, 2003. ISBN: 978-0080535418
- [17] Kreidler ER, Hummel FA. The crystal chemistry of apatite: Structure fields of fluor- and chlorapatite. *Journal of Physics and Chemistry of Solids* 2007;68 1863–1871
- [18] Klement R. Isomorphic replacement of phosphorus in apatites by silicon and sulfur. *Naturwissenschaften* 1939;27 57–58.
- [19] Pasero M, Kampf AR, Ferraris C, Pekov IV, Rakovan JR, White TJ. Nomenclature of the apatite supergroup minerals. *European Journal of Mineralogy* 2010;22 163–179.
- [20] Que M, Ci Z, Wang Y, Zhu G, Xin S, Shi Y, Wang Q. Crystal structure and luminescence properties of a cyan emitting  $\text{Ca}_{10}(\text{SiO}_4)_3(\text{SO}_4)_3\text{F}_2\text{:Eu}^{2+}$  phosphor. *Crystal Engineering Communications* 2013;15 6389–6394. DOI: 10.1039/C3CE40482J
- [21] Fang YN, Ritter C, White TJ. Crystal chemical characteristics of ellestadite-type apatite: implications for toxic metal immobilization. *Dalton Transactions* 2014;43(42) 16031–16043. DOI: 10.1039/c4dt02088j
- [22] Fang Y, Ritter C, White T. The crystal chemistry of  $\text{Ca}_{10-y}(\text{SiO}_4)_3(\text{SO}_4)_3\text{Cl}_{2-x-2y}\text{F}_x$  ellestadite. *Inorganic Chemistry* 2011;50(24) 12641–12650. DOI: 10.1021/ic201673r.
- [23] Balachandran PV, Rajan K. Structure maps for  $\text{Al}_4\text{AlI}_6(\text{BO}_4)_6\text{X}_2$  apatite compounds via data mining. *Acta Crystallographica Section B* 2012;68(1) 24–33.
- [24] Hughes JM, Cameron M, Crowley KD. Ordering of divalent cations in the apatite structure; crystal structure refinements of natural Mn- and Sr-bearing apatite. *American Mineralogist* 1991;76 1857–1862.
- [25] O'Donnell MD, Fredholm Y, de Rouffignac A, Hill RG. Structural analysis of a series of strontium-substituted apatites. *Acta Biomaterialia* 2008;4(5) 1455–1464.
- [26] Hill RG, Stamboulis A, Law RV, Clifford A, Towler MR, Crowley C. The influence of strontium substitution in fluorapatite glasses and glass-ceramics. *Journal of Non-Crystalline Solids* 2004;336(3) 223–229.

- [27] Suchanek WL, Byrappa K, Shuk P, Riman RE, Janas VF, Ten Huysen KS. Preparation of magnesium-substituted hydroxyapatite powders by the mechanochemical-hydrothermal method. *Biomaterials* 2004;25(19) 4647–4657.
- [28] Lijuan X, Liuyun J, Lixin J, Chengdong X. Synthesis of Mg-substituted hydroxyapatite nanopowders: Effect of two different magnesium sources. *Materials Letters* 2013;106 246–249.
- [29] Shanmugam S, Gopal B. Copper substituted hydroxyapatite and fluorapatite: Synthesis, characterization and antimicrobial properties. *Ceramics International* 2014;40(10) 15655–15662.
- [30] Mobasherpour I, Salahi E, Pazouki M. Removal of nickel (II) from aqueous solutions by using nano-crystalline calcium hydroxyapatite. *Journal of Saudi Chemical Society* 2011;15(2) 105–112.
- [31] Shepherd D. Zinc-Substituted Hydroxyapatite for the Inhibition of Osteoporosis Hydroxyapatite (Hap) for Biomedical Applications. Woodhead Publishing, 2015. ISBN: 978-1-78242-033-0
- [32] Ren F, Xin R, Ge X, Leng Y. Characterization and structural analysis of zinc-substituted hydroxyapatites. *Acta Biomaterialia* 2009;5(8) 3141–3149.
- [33] Miyaji F, Kono Y, Suyama Y. Formation and structure of zinc-substituted calcium hydroxyapatite. *Materials Research Bulletin* 2005;40(2) 209–220.
- [34] Kramer ER, Morey AM, Staruch M, Suib SL, Jain M, Budnick JL, Wei M. Synthesis and characterization of iron-substituted hydroxyapatite via a simple ion-exchange procedure. *Journal of Materials Science* 2013;48(2) 665–673.
- [35] Kramer E, Itzkowitz E, Wei M. Synthesis and characterization of cobalt-substituted hydroxyapatite powders. *Ceramics International* 2014;40(8) 13471–13480.
- [36] Anderson JB, Kostiner E. The crystal structure of cobalt-substituted calcium chlorapatite. *Journal of Solid State Chemistry* 1987;66(2) 343–349.
- [37] Fleet ME, Pan Y. Site preference of rare earth elements in fluorapatite. *American Mineralogist* 1995;80 329–335.
- [38] Hughes JM, Cameron M, Mariano AN. Rare-earth-element ordering and structural variations in natural rare-earth-bearing apatites. *American Mineralogist* 1991;76 1165–1173.
- [39] Cornwall HR. B065: Mineral and Water Resources of Nevada. Vydavatel NV Bureau of Mines & Geology, 1964.
- [40] Connelly NG. IUPAC Recommendations 2005. Royal Society of Chemistry (Great Britain), International Union of Pure and Applied Chemistry, 2005. ISBN: 978-0854044382
- [41] Letcher TM, Scott JL, Peter L. Materials for a Sustainable Future. Royal Society of Chemistry, 2012. ISBN: 978-1849734073

- [42] Kothe E, Varma A. Bio-Geo Interactions in Metal-Contaminated Soils. Soil Biology — Volume 31. Springer Science & Business Media, 2012. ISBN: 978-3642233272
- [43] Seaborg GT, Katz JJ, Morss LR. The Chemistry of the Actinide Elements, Volume 2. 2nd ed., Springer Science & Business Media, 2012. ISBN: 978-9400931558
- [44] Get'man EI, Marchenko VI, Loboda SN, Yablochkova NV. Substitutions of neodymium for strontium in the  $\text{Sr}_5(\text{VO}_4)_3\text{OH}$  structure. Russian Journal of Inorganic Chemistry 2007;52(2) 147–149.
- [45] Report of the Twelfth Annual Meeting of the National Research Council, Washington D.C. 1969. National Research Council (U.S.), National Academies, 1969.
- [46] Natrajan LS, Swinburne AN, Andrews MB, Randall S, Heath SL. Redox and environmentally relevant aspects of actinide(IV) coordination chemistry. Coordination Chemistry Reviews 2014;266-267 171-193.
- [47] Luo Y, Hughes JM, Rakovan J, Pan YM. Site preference of U and Th in Cl, F, and Sr apatites. American Mineralogist 2009;94 345–351.
- [48] Riadh QE, Cohen-Adad M, Goutaudier C, Panczer G. Uranium-doped britholites  $\text{Ca}_x\text{La}_y(\text{SiO}_4)_{6-u}(\text{PO}_4)_u\text{O}_t\text{:U}$  synthesis, characterization and preliminary study of uranium diffusion. Solid State Ionics 2005;176(1) 225–231.
- [49] Terra O, Audubert F, Dacheux N, Guy C, Podor R. Synthesis and characterization of uranium-bearing britholites. Journal of Nuclear Materials 2007;366(1-2) 70–86.
- [50] Terra O, Audubert F, Dacheux N, Guy C, Podor R. Synthesis and characterization of thorium-bearing britholites. Journal of Nuclear Materials 2006;354(1-3) 49–65.
- [51] Lim PN, Chang L, Thian ES. Development of nanosized silver-substituted apatite for biomedical applications: A review. Nanomedicine: Nanotechnology, Biology and Medicine 2015;11(6) 1331–1344.
- [52] Nounah A, Lacout JL, Savariault JM. Localization of cadmium in cadmium-containing hydroxy- and fluorapatites. Journal of Alloys and Compounds 1992;188 141–146.
- [53] Badraoui B, Aissa A, Bigi A, Debbabi M, Gazzano M. Synthesis and characterization of  $\text{Sr}_{(10-x)}\text{Cd}_x(\text{PO}_4)_6\text{Y}_2$  (Y = OH and F): A comparison of apatites containing two divalent cations. Materials Research Bulletin 2009;44(3) 522–530.
- [54] Grisafe DA, Hummel FA. Pentavalent ion substitutions in the apatite structure part A. Crystal chemistry. Journal of Solid State Chemistry 1970;2(2) 160–166.
- [55] Lee YK, Stephens PW, Tang Y, Li W, Phillips BL, Parise JB, Reeder RJ. Arsenate substitution in hydroxylapatite: Structural characterization of the  $\text{Ca}_5(\text{P}_x\text{As}_{1-x}\text{O}_4)_3\text{OH}$  solid solution. American Mineralogist 2009;94 666–675
- [56] Zhu Y, Zhang X, Long F, Liu H, Qian M, He N. Synthesis and characterization of arsenate/phosphate hydroxyapatite solid solution. Materials Letters 2009;63(13-14) 1185–1188.



- [57] Tilley RJD. Understanding Solids: The Science of Materials. 2nd ed., New York: John Wiley & Sons, 2013. ISBN: 978-1-118-42328-8
- [58] George G, Gupta SK, Rao PVR, Narasaraaju TSB. Preparation and characterization of phosphate and arsenate apatites of strontium and their solid solutions. *Journal of Materials Science* 1987;22 2274–2276.
- [59] Bell AMT, Henderson CMB, Wendlandt RF, Harrisonc WJ. Rietveld refinement of  $\text{Sr}_5(\text{AsO}_4)_3\text{Cl}$  from high-resolution synchrotron data. *Acta Crystallographica Section E* 2009;65 i16–i17.
- [60] Mugavero SJ, Bharathy M, McAlum J, Loye HC. Crystal growth of alkaline earth vanadates from hydroxide fluxes. *Solid State Sciences* 2008;10 370–376.
- [61] Chernorukov NG, Knyazev AV, Bulanov EN. Isomorphism and phase diagram of the  $\text{Pb}_5(\text{PO}_4)_3\text{Cl}$ - $\text{Pb}_5(\text{VO}_4)_3\text{Cl}$  system. *Russian Journal of Inorganic Chemistry* 2010;55(9) 1463–1470.
- [62] Glasser FP, Osborn EF. Phase equilibrium studies in the system  $\text{CaO}$ - $\text{Cr}_2\text{O}_3$ - $\text{SiO}_2$ . *Journal of the American Ceramic Society* 1958;41 358–367.
- [63] Klemm W. Anomale Wertigkeiten. *Angewandte Chemie* 1951;63(17-18) 396–402.
- [64] Scholder R, Klemm W. Über neue Metallate mit Sauerstoff und Fluor als Liganden. *Angewandte Chemie* 1954;66 461–474.
- [65] Scholder R, Suchy H. *Zeitschrift für anorganische und allgemeine Chemie* 1961;308 295.
- [66] Scholder R, Schwarz H. Z. Über Alkalichromate(V). *Zeitschrift für anorganische und allgemeine Chemie* 1963;326(1-2) 1–10.
- [67] Banks E, Jaunarajs KL. Chromium analogs of apatite and spodiosite. *Inorganic Chemistry* 1965;1(4) 78–83.
- [68] Scholder R, Schwochow F, Schwarz H. Über Alkalichromate(V). *Zeitschrift für anorganische und allgemeine Chemie* 1968;363(1-2) 10–23.
- [69] Banks E, Greenblatt M, McGarvey BR. Electron spin resonance of  $\text{CrO}_4^{3-}$  in chloroapatite  $\text{Ca}_5(\text{PO}_4)_3\text{Cl}$ . *Journal of Solid State Chemistry* 1971;3(2) 308–313.
- [70] Guldotti RA, Roth EP. Specific heats of calcium chromate chlorides, calcium chromate hydroxide and calcium chromate ( $\text{Ca}_5(\text{CrO}_4)_3\text{Cl}$ ,  $\text{Ca}_2\text{CrO}_4\text{Cl}$ ,  $\text{Ca}_5(\text{CrO}_4)_3\text{OH}$ , and  $\text{Ca}(\text{CrO}_4)$  at elevated temperatures. *Journal of Chemical & Engineering Data* 1985;30(3) 328–329.
- [71] Baikie T, Ahmad Z, Srinivasan M, Maignan A, Pramana SS, White TJ. The crystallographic and magnetic characteristics of  $\text{Sr}_2\text{CrO}_4$  ( $\text{K}_2\text{NiF}_4$ -type) and  $\text{Sr}_{10}(\text{CrO}_4)_6\text{F}_2$  (apatite-type). *Journal of Solid State Chemistry* 2007;180(5) 1538–1546.
- [72] Wu P, Zeng YZ, Wang CM. Prediction of apatite lattice constants from their constituent elemental radii and artificial intelligence methods. *Biomaterials* 2004;25(6) 1123–1130.

- [73] Ford WF, Rees WJ. The CaO-MgO-Cr<sub>2</sub>O<sub>3</sub> ternary system: Part I. Partial investigation of the CaO-Cr<sub>2</sub>O<sub>3</sub> system. *Transactions of the British Ceramic Society* 1948;47(6) 207–231.
- [74] Ford WF, Rees WJ. The CaO-MgO-Cr<sub>2</sub>O<sub>3</sub> ternary system: Part II. Further experiments. *Transactions of the British Ceramic Society* 1949;48(8) 291–312.
- [75] Ford WF, White J. The CaO-MgO-Cr<sub>2</sub>O<sub>3</sub> ternary system. Part III. CaO-CrO<sub>3</sub>-Cr<sub>2</sub>O<sub>3</sub> ternary and the MgO-Cr<sub>2</sub>O<sub>3</sub> and CaO-MgO binary systems. *Transactions of the British Ceramic Society* 1949;48 417–428.
- [76] Tyutyunnik AP, Bazuev GV. Synthesis, crystal structure and magnetic properties of Sr<sub>5</sub>(CrO<sub>4</sub>)<sub>3</sub>(Cu<sub>0.586</sub>O) with apatite-like structure. *Journal of Alloys and Compounds* 2012;522 141–143.
- [77] Wang Y, Ma J, Zhou L, Chen J, Liu Y, Qiu Z, Zhang S. Dual functional selenium-substituted hydroxyapatite, *Interface Focus* 2012;2(3) 378–386.
- [78] Monteil-Rivera F, Masset S, Dumonceau J, Fedoroff M, Jeanjean J. Sorption of selenite ions on hydroxyapatite. *Journal of Materials Science Letters* 1999;18(14) 1143–1145.
- [79] Kolmas J, Oledzka E, Sobczak M, Nałęcz-Jawecki G. Nanocrystalline hydroxyapatite doped with selenium oxyanions: A new material for potential biomedical applications. *Materials Science and Engineering C* 2014;39 134–142.
- [80] Zhang W, Chai Y, Cao N, Wang Y. Synthesis and characterization of selenium substituted hydroxyapatite via a hydrothermal procedure. *Materials Letters* 2014;134 123–125.
- [81] Derek EC. *Chemistry, Biochemistry and Technology*. 6th ed., CRC Press, 2013. ISBN: 978-1439840887
- [82] Habelitz S, Pascual L, Durán A. Transformation of tricalcium phosphate into apatite by ammonia treatment. *Journal of Materials Science* 2001;36(17) 4131–4135.
- [83] Vandecandelaere N, Bosc F, Rey C, Drouet C. Peroxide-doped apatites: Preparation and effect of synthesis parameters. *Powder Technology* 2014;255 3–9.
- [84] Dugas J, Rey C. Electron spin resonance characterization of superoxide ions in some oxygenated apatites. *The Journal of Physical Chemistry* 1977;81(14) 1417–1419.
- [85] Yu H, Zhang H, Wang X, Gu Z, Li X, Deng F. Local structure of hydroxy-peroxy apatite: A combined XRD, FT-IR, Raman, SEM, and solid-state NMR study. *Journal of Physics and Chemistry of Solids* 2007;68(10) 1863–1871.
- [86] Zhao H, Li X, Wang J, Qu S, Weng J, Zhang X. Characterization of peroxide ions in hydroxyapatite lattice. *Journal of Biomedical Materials Research* 2000;52(1) 157–163.
- [87] Bouroushian M. *Electrochemistry of Metal Chalcogenides*. Monographs in Electrochemistry. Springer Science & Business Media, 2010. ISBN: 978-3642039676
- [88] Henning PA, Adolfsson E, Grins J. The chalcogenide phosphate apatites Ca<sub>10</sub>(PO<sub>4</sub>)<sub>6</sub>S, Sr<sub>10</sub>(PO<sub>4</sub>)<sub>6</sub>S, Ba<sub>10</sub>(PO<sub>4</sub>)<sub>6</sub>S and Ca<sub>10</sub>(PO<sub>4</sub>)<sub>6</sub>Se. *Zeitschrift für Kristallographie* 2000;215 226–230.

- [89] Chen S, Hoffmann S, Carrillo-Cabrera W, Akselrud LG, Prots Y, Schwarz U, Zhao Jing-T, Kniep R.  $\text{Sr}_{10}[(\text{PO}_4)_{5.5}(\text{BO}_4)_{0.5}](\text{BO}_2)$ : Growth and crystal structure of a strontium phosphate orthoborate metaborate closely related to the apatite-type crystal structure. *Journal of Solid State Chemistry* 2010;183(3) 658–661.
- [90] Chen S, Hoffmann S, Carrillo-Cabrera W, Akselrud LG, Prots Y, Zhao Jing-T, Kniep R. FA2-MS01-P20:  $\text{Sr}_{10}(\text{PO}_4)_{5.5}(\text{BO}_4)_{0.5}(\text{BO}_2)$ : A strontium borate-phosphate closely related to the apatite crystal structure. *Acta Crystallographica* 2009;A65 182.
- [91] Calvo C, Faggiani R, Krishnamurthy N. The crystal structure of  $\text{Sr}_{9.402}\text{Na}_{0.209}(\text{PO}_4)_6\text{B}_{0.996}\text{O}_2$  — A deviant apatite. *Acta Crystallographica* 1975;31 B 188-192.
- [92] Nickel EH. Solid solution in mineral nomenclature. *Canadian Mineralogist* 1992;30 231–234.
- [93] Hughes JM, Cameron M, Crowley KD. Crystal structures of natural ternary apatites: Solid solution in the  $\text{Ca}_5(\text{PO}_4)_3\text{X}$  (X = F, OH, Cl) system. *American Mineralogist* 1990;75 295–304.
- [94] Schlesinger MI, Hlavác V. Ten Lectures on Statistical and Structural Pattern Recognition. Computational Imaging and Vision — Volume 24. Springer Science & Business Media, 2013. ISBN: 978-9401732178
- [95] Banasik K, Galuskin EV, Armbruster T, Lazic B, Galuskina IO, Gazeev VM. Apatite supergroup minerals of the solid solution  $\text{Ca}_5[(\text{PO}_4)_{3-x}(\text{AsO}_4)_x]_{\oplus 3-2y}[(\text{SO}_4)_y(\text{SiO}_4)_y]_{\oplus 2y}(\text{OH}, \text{F}, \text{Cl})$ ,  $x = 0-3$ ,  $y = 0-1.5$ , from high temperature skarn of the Upper Chegem caldera, Northern Caucasus, Russia. *European Mineralogical Conference 2012*, Vol. 1, EMC2012-298, 2012.
- [96] Wright FE. On three contact minerals from Valardeña, Durango, Mexico (Gehlenite, spurrite and hillebrandite). *American Journal of Science* 1908;176 545–554.
- [97] Bournon JL. Humite, in *Catalogue de la Collection Minéralogique du Compte de Bournon, De l'imprimerie de R. Juigné* (London) 1813; 52-54.
- [98] Tilley CE. On larnite (calcium orthosilicate, a new mineral) and its associated minerals from the limestone-contact zone of Scawt Hill, Co. Antrim. *Mineralogical Magazine* 1929;22 77–86.
- [99] Li X, Xu W, Wang S, Tang M, Shen X. Effect of  $\text{SO}_3$  and MgO on Portland cement clinker: Formation of clinker phases and alite polymorphism. *Construction and Building Materials* 58;2014 182–192.
- [100] Fukuda K, Ito S, Taguchi H. Thermoelasticity of belite in Portland cement clinker. *Cement and Concrete Research* 1998;28(8) 1141–1145.
- [101] Hjorth L, Laurén K-G. Belite in Portland cement. *Cement and Concrete Research* 1971;1(1) 27–40.

- [102] Hamm HM, Hentschel G. Reinhardbraunsite,  $\text{Ca}_5(\text{SiO}_4)_2(\text{OH},\text{F})_2$ , a new mineral — The natural equivalent of synthetic "calcio-chondrodite". *Neues Jahrbuch für Mineralogie, Monatshefte* 1983; 119-129.
- [103] Galuskin EV, Gazeev VM, Lazic B, Armbruster T, Galuskina IO, Zadov AE, Pertsev NN, Wrzalik R, Dzierzanowski P, Gurbanov AG, Bzowska G. Chegemite  $\text{Ca}_7(\text{SiO}_4)_3(\text{OH})_2$  — A new humite group calcium mineral from the northern Caucasus, Kabardino-Balkaria, Russia. *European Journal of Mineralogy* 2009;21 1045–1059.
- [104] Tsukimura K, Kanazawa Y, Aoki M, Bunno M. Structure of wadalite  $\text{Ca}_6\text{Al}_5\text{Si}_2\text{O}_{16}\text{Cl}_3$ . *Acta Crystallographica* 1993;C49 205–207.
- [105] Mihajlovic T, Lengauer CL, Ntaflos T, Lolitsch U, Tillmanns E. Two new minerals, rondorfite,  $\text{Ca}_8\text{Mg}[\text{SiO}_4]_4\text{Cl}_2$ , and almarudite,  $\text{K}(\square, \text{Na})_2(\text{Mn}, \text{Fe}, \text{Mg})_2(\text{Be}, \text{Al})_3[\text{Si}_{12}\text{O}_{30}]$ , and a study of iron-rich wadalite,  $\text{Ca}_{12}[(\text{Al}_8\text{Si}_4\text{Fe}_2)\text{O}_{32}]\text{Cl}_6$ , from the Bellerberg (Bellberg) volcano, Eifel, Germany. *Neues Jahrbuch für Mineralogie, Abhandlungen* 2004;179 265–294.
- [106] Scacchi A. Della cuspidina e del neocrisolito, nuovi minerali vesuviani, *Rendiconto dell'Accademia delle Scienze Fisiche e Matematiche (sezione della Societa reale di Napoli)* 1876;15, 208-209.
- [107] Galuskin EV, Gazeev VM, Armbruster T, Zadov AE, Galuskina IO, Pertsev NN, Dzierzanowski P, Kadiyski M, Gurbanov AG, Wrzalik R, Winiarski A. Lakargiite  $\text{CaZrO}_3$ : A new mineral of the perovskite group from the North Caucasus, Kabardino-Balkaria, Russia. *American Mineralogist* 2008;93 1903–1910.
- [108] Chesnokov BV, Bazhenova LF. Srebrodolskite  $\text{Ca}_2\text{Fe}_2\text{O}_5$  — A new mineral, *Zapiski Vsesoyuznogo Mineralogicheskogo Obshchestva* 1985;114(2) 195–199.
- [109] Nöggerath JJ. Sanidin, in *Mineralogische Studien über die Gebirge am Niederrhein*. Johann Christian Hermann (Frankfurt) 1808; 24-39.
- [110] Newnham RE, de Haan YM. Refinement of the  $\alpha\text{-Al}_2\text{O}_3$ ,  $\text{Ti}_2\text{O}_3$ ,  $\text{V}_2\text{O}_3$  and  $\text{Cr}_2\text{O}_3$  structures. *Zeitschrift für Kristallographie* 1962;117 235–237.
- [111] Gibbs GV. The polymorphism of cordierite I: The crystal structure of low cordierite. *American Mineralogist* 1966;51 1068–1087.
- [112] Winter JK, Subrata Ghose. Thermal expansion and high-temperature crystal chemistry of the  $\text{Al}_2\text{SiO}_5$  polymorphs. *American Mineralogist* 1979;64 573–586.
- [113] Wright FE. On three contact minerals from Valardeña, Durango, Mexico. (gehlenite, spurrite and hillebrandite). *American Journal of Science* 1908;176, 545–554.
- [114] Parry J, Wright FE. Afwillite, a new hydrous calcium silicate, from Dutoitspan mine, Kimberley, South Africa. *Mineralogical Magazine* 1925;20 277–285.
- [115] Parry J, Williams AF, Wright FE. On bultfonteinite, a new fluorine-bearing hydrous calcium silicate from South Africa. *Mineralogical Magazine* 1932;23 145–162.

- [116] Grew ES, Locock A, Mills SJ, Galuskina IO, Galuskin EV, Hälenius U. Nomenclature of the garnet supergroup. *American Mineralogist* 2013;98(4) 785–811.
- [117] Lehmann J. Über den ettringit, ein neues mineral, in Kalkeinschlüssen der Lava von Ettringen (Laacher Gebiet). *Neues Jahrbuch für Mineralogie, Geologie und Palaontologie* 1874; 273–275.
- [118] Onda A, Ogo S, Kajiyoshi K, Yanagisawa K. Hydrothermal synthesis of vanadate/phosphate hydroxyapatite solid solutions. *Materials Letters* 2008;62(8-9) 1406–1409.
- [119] Sugiyama S, Osaka T, Hirata Y, Sotowa Ken-I. Enhancement of the activity for oxidative dehydrogenation of propane on calcium hydroxyapatite substituted with vanadate. *Applied Catalysis A: General* 2006;312 52–58.
- [120] Piotrowski A, Kahlenberg V, Fischer RX. The solid solution series of the sulfate apatite system  $\text{Na}_{6.45}\text{Ca}_{3.55}(\text{SO}_4)_6(\text{F}_x\text{Cl}_{1-x})_{1.55}$ . *Journal of Solid State Chemistry* 2002;163(2) 398–405.
- [121] Bajda T, Mozgawa W, Manecki M, Flis J. Vibrational spectroscopic study of mimetite–pyromorphite solid solutions. *Polyhedron* 2011;30(15) 2479–2485.
- [122] Mayer I, Cohen S, Matalon JR. Solid solutions of  $\text{Pb}_8\text{M}_2(\text{XO}_4)_6$  lead alkali apatites. *Journal of Solid State Chemistry* 1981;36(3) 271–274.
- [123] Peck WH, Tumpane KP. Low carbon isotope ratios in apatite: An unreliable biomarker in igneous and metamorphic rocks. *Chemical Geology* 2007;245(3-4) 305–314.
- [124] Eagle R, Schauble EA, Tripathi AK, Fricke HC, Tuetken T, Eiler JM. A paleothermometer based on abundances of  $^{13}\text{C}$ - $^{18}\text{O}$  bonds in bioapatite: Calibration and reconstruction of the body temperatures of extinct Cenozoic mammals and Mesozoic dinosaurs. *American Geophysical Union, Fall Meeting 2009*, abstract #PP31B-1342.
- [125] Trappe J. Phanerozoic Phosphorite Depositional Systems: A Dynamic Model for a Sedimentary Resource System. *Lecture Notes in Earth Sciences — Volume 76*, ISSN 0930-0317. Springer, 1998. ISBN: 978-3540696049
- [126] Teodorovich GI. *Authigenic Minerals in Sedimentary Rocks*. Springer Science & Business Media, 2012. ISBN: 978-1468406528
- [127] Grossan EL. Applying oxygen isotope paleothermometry in deep time. *The Paleontological Society Papers* 2012;18 39–67.
- [128] LaPorte DF, Holmden C, Patterson WP, Prokopiuk T, Eglington BM. Oxygen isotope analysis of phosphate: improved precision using TC/EA CF-IRMS. *Journal of Mass Spectrometry* 2009;44(6) 879–890.
- [129] Kohn MJ, Cerling TE. Stable isotope compositions of biological apatite. *Reviews in Mineralogy and Geochemistry* 2002;48 455–488.
- [130] Land LS, Lundelius EL Jr., Valastro S. Isotopic ecology of deer bones. *Palaeogeography, Palaeoclimatology, Palaeoecology* 1980;32 143–151.



- [131] Ericson JE, Sullivan CH, Boaz NT. Diets of Pliocene mammals from Omo, Ethiopia, deduced from carbon isotopic ratios in tooth apatite. *Palaeogeography, Palaeoclimatology, Palaeoecology* 1981;36 69–73.
- [132] Sullivan CH, Krueger HW. Carbon isotope analysis of separate chemical phases in modern and fossil bone. *Nature* 1981;292 333–335.
- [133] Lee-Thorp JA, van der Merwe NJ. Carbon isotope analysis of fossil bone apatite. *South African Journal of Science* 1987;83 712–715.
- [134] Lee-Thorp JA, Sealy JC, van der Merwe NJ. Stable carbon isotope ratio differences between bone collagen and bone apatite, and their relationship to diet. *Journal of Archaeological Science* 1989;16 585–599.
- [135] Reynard B, Balter V. Trace elements and their isotopes in bones and teeth: Diet, environments, diagenesis, and dating of archeological and paleontological samples. *Palaeogeography, Palaeoclimatology, Palaeoecology* 2014;416 4–16.
- [136] O'Connell JP, Haile JM. *Thermodynamics: Fundamentals for Applications*. Cambridge University Press, 2005. ISBN: 978-1139443173
- [137] Brice JC. Some thermodynamic aspects of the growth of strained crystals. *Journal of Crystal Growth* 1975;28 249–253.
- [138] Almora-Barrios N, Grau-Crespo R, de Leeuw NH. A computational study of magnesium incorporation in the bulk and surfaces of hydroxyapatite. *Langmuir* 29;2013 5851–5856.
- [139] Rabone JAL, De Leeuw NH. Interatomic potential models for natural apatite crystals: Incorporating strontium and the lanthanides. *Journal of Computational Chemistry* 2006;27 253–266.
- [140] Davranche M, Pourret O, Gruau G, Dia A, Le Coz-Bouhnik M. Adsorption of REE(III)-humate complexes onto MnO<sub>2</sub>: experimental evidence for cerium anomaly and lanthanide tetrad effect suppression. *Geochimica et Cosmochimica Acta* 2005;69, 4825–4835.
- [141] Cherniak DJ. Rare earth element diffusion in apatite. *Geochimica et Cosmochimica Acta* 2000;64 3871–3885.
- [142] Cherniak DJ. Uranium and manganese diffusion in apatite. *Chemical Geology* 2005;219(1-4) 297–308.